Simulation of rockfall generated seismic signals and the influence of surface topography

J. Kuehnert[1], A. Mangeney[1], Y. Capdeville[2], J. P. Métaxian[1], L. F. Bonilla[3], E. Stutzmann[1], E. Chaljub[4], P. Boissier[1,5], C. Brunet[1,5], P. Kowalski[1,5], F. Lauret[1,5], Clément Hibert[6]

[1]Université de Paris, Institut de Physique du Globe de Paris, CNRS, F-75005 Paris, France
[2]Laboratoire de Planétologie et Géodynamique, UMR CNRS 6112, Université de Nantes,44300 Nantes, France
[3]Université Gustave Eiffel, Marne-la-Vallée, France
[4]Univ. Grenoble Alpes, Univ. Savoie Mont Blanc, CNRS, IRD, IFSTTAR, ISTerre, 38000 Grenoble, France
[5]Observatoire Volcanologique du Piton de la Fournaise/Institut de Physique du Globe de Paris, CNRS UMS 3454 & UMR 7154, Sorbonne Paris Cité, La Plaine des Cafres, Réunion Island, France
[6]Université de Strasbourg, CNRS, EOST/IPGS UMR 7516, F-67000 Strasbourg

Key Points:

- First-ever simulation of high frequency rockfall seismic waves using the 3D Spectral Element Method
- Volcano topography induced ground motion amplification depends on soil properties and rockfall position
- Simulations and observations are successfully compared by means of inter-station spectral ratios and Hertz theory

Corresponding author: Julian Kuehnert, `kuehnert@ipgp.fr`

Abstract

Rockfalls seismic waves contain valuable information on event properties. However, as rockfalls predominately occur in mountainous regions, generated seismic waves are prone to be affected by strong surface topography. For this reason, the influence of topography on the wavefield, in particular surface wave propagation, is investigated using the Spectral Element Method on a 3D domain with realistic surface topography of Dolomieu crater on Piton de la Fournaise volcano, La Réunion. Topography induced ground motion modification is studied relative to a flat reference model. Peak Ground Velocity (PGV) and total kinetic energy can be (de-)amplified by factors up to 10 and 20, respectively. The spatial distribution of the amplification is strongly influenced by the underlying geology as shallow low velocities guide energy along the surface. Simulations on different topographies suggest that the wavefield is affected more by variations of crater curvature than crater depth.

To reveal the effect of topography on recorded signals at Dolomieu crater, interstation spectral ratios are computed. It is demonstrated that these ratios can only be simulated when taking into account surface topography while the comparisons suggest that the direction of the acting source and the resulting radiation patterns can be ignored.

Finally, the seismic signature of single impacts is studied. Comparison with simulations help to associate signal pulses to impact sources. It is revealed that a single impact can provoke complex waveforms of multiple peaks, especially when considering topography. Impact forces derived from Hertz contact theory result in comparable magnitudes of real and simulated signal amplitudes.

1 Introduction

The interaction of the seismic wave field with complex surface geometries can locally modify the seismic ground motion. Anomalously strong shaking on hill tops, mountain ridges or flanks causing severe structural damages at buildings (W. H. K. Lee et al., 1994; Hartzell et al., 1994; Hough et al., 2010) or triggering earthquake-induced landslides (Meunier et al., 2008; Harp et al., 2014) have been related to seismic amplification due to this topographic effect. Data from field experiments support the assumption of amplified ground motion at the mountain top relative to its base (Davis & West, 1973; Pedersen et al., 1994; Spudich et al., 1996).

Numerous studies have tried to quantify numerically the topographic effect on seismic waves generated by deep sources in order to better understand and predict site specific ground motion. Geli et al. (1988) compiled previous results from experimental and theoretical studies with new results of more complex models (i.e. including subsurface layering and neighboring ridges), trying to explain the underestimation of amplification factors in previous numerical simulations. Besides confirming significant amplification at hill tops for wavelengths comparable to the mountain width, they express the need of more complex, three-dimensional models. Bouchon and Barker (1996), simulating the ground motion after the 1994 Northridge, California, earthquake on a homogeneous model with three-dimensional topography, point out that a small hill of less than 20-m high can amplify ground acceleration by 30% to 40% for frequencies between 2 Hz and 15 Hz. S. J. Lee, Chan, et al. (2009) model the seismic response of the mountainous region of Yangmingshan, Taiwan, using the 3D spectral element method and a detailed representation of the topography. They find that values of Peak Ground Acceleration (PGA) can be increased up to 100% relative to simulations on a flat surface. Additionally, they report an increase of up to 200% in cumulative kinetic energy as a result of increased duration of shaking due to complex reflection and scattering processes of the seismic waves at the topography.

Yet, due to complex patterns of amplification and deamplification it is difficult to quantify the effect of topography in a generic way. Maufroy et al. (2015) propose to use the topography curvature, smoothed in dependency of the studied wavelength, as proxy for amplification factors. They confirm correlation between the smoothed curvature and

topographic amplification using a database of 200 earthquake ground-motion simulations. Based on the NGA-West2 earthquake catalog (Ancheta et al., 2014), Rai et al. (2017) show statistical biases of site residuals in the ground motion prediction equation (GMPE) presented by Chiou and Youngs (2014) towards relative elevation and smoothed curvature and suggest topographic modification factors dependent on signal frequency and relative elevation. Besides these successful findings, some authors point out the complex coupling between topography and the underlying soil structure which must not be neglected when estimating topographic amplification (Assimaki & Jeong, 2013; Hailemikael et al., 2016; B. Wang et al., 2018; Jeong et al., 2019).

All the studies mentioned above investigate topographic effects on a seismic wave field of vertical incidence. S. J. Lee, Komatitsch, et al. (2009) investigates the influence of the source depth on ground motion amplification and demonstrates that amplification in a basin can be reduced when a mountain range is located in between the basin and a shallow source. This suggests that surface topography can have a pronounced influence on the propagation of surface waves as they are subjected to an accumulated effect of scattering, diffraction, reflection and conversion. It is crucial to enhance understanding of these mechanisms for the study of shallow seismic sources which have gained increasing attention with the emerging field of environmental seismology (Larose et al., 2015). Several authors investigate numerically the interaction of surface waves with 2D surface geometries such as corners, hills or canyons (Fuyuku & Matsumoto, 1980; Weaver, 1982; Snieder, 1986; Sánchez-Sesma & Campillo, 1993; Zhang et al., 2018; B. Wang et al., 2018). Ma et al. (2007) demonstrate that a topographic feature 10 times smaller than the wavelength can still considerably reduce the amplitude of by-passing surface waves. Similar to S. J. Lee, Komatitsch, et al. (2009), they simulate on a 3D model of San Gabriel Mountains, Los Angeles, California, the shielding effects of large-scale topography on fault-generated surface waves, finding amplification factors in peak ground velocity (PGV) of up to +50 % on the source-side of the mountain range and up to -50 % on the opposite site. L. Wang et al. (2015) model the influence of an uplifted and a depressed topography on the wave field generated by a vertical point source at the surface above a 2D homogeneous half space. Comparing amplitudes and frequency content between source side and far source side they find that the depressed topography causes stronger contrasts than the uplifted topography, especially for steeper slopes and at higher frequencies.

The present study is focused on seismic waves generated by rockfalls. Different to the source mechanism of earthquakes, rockfall seismic sources can generally be described by force impulses on the Earth's surface. Seismic signals from rockfalls, or more generally from landslides, have been demonstrated to be of great usefulness in order to classify and locate events as well as constrain flow dynamics and rheology (e.g. Vilajosana et al., 2008; Deparis et al., 2008; Favreau et al., 2010; Hibert et al., 2011; Dammeier et al., 2011; Moretti et al., 2012; Bottelin et al., 2014). However, as landslides predominantly occur in areas of strong topographic relief, the measurements are prone to be strongly influenced by topography variations which can lead to erroneous landslide estimates. For example, in order to calculate landslide volumes, the generated seismic energy is estimated from seismic recordings (Hibert et al., 2011). At the same time, energy estimations can vary from station to station. We will show here that topography can partly explain relative signal amplitudes between seismic stations.

In the following we will introduce the study site located at Dolomieu crater on Piton de la Fournaise volcano, La Réunion. First of all, an exemplary rockfall event at Dolomieu crater is presented by means of camera images and recorded seismic signals. Then, the numerical model for the SEM simulations will be defined which entails a discussion on the seismic velocity profile of Piton de la Fournaise. After setting up the Earth model, the simulated wave propagation is studied on different velocity models. Using a reference model with flat surface, topography induced amplification patterns regarding peak ground velocity (PGV) and total kinetic energy are computed. By this, the influence of the underlying velocity model is shown. Additionally, amplification patterns from a horizontal seismic source is discussed. As the resolution of topography on the numerical do-

mains is limited, synthetic seismograms are compared on models with different topography resolutions. Also, similar to authors of previous studies who try to quantify the effect of topography in terms of its geometric parameters, as for example canyon width over canyon depth (L. Wang et al., 2015) or frequency-scaled curvature (Maufroy et al., 2015), the influence of crater depth and its curvature on ground motion is investigated.

Finally, real seismic signals generated by rockfalls at Dolomieu crater are analyzed. To begin, simulated and observed spectral ratios between seismic stations are compared. The ratios allow to investigate the spectral content of the signals independently of the rockfall source. The aim is to find out, whether the spectral ratios are characteristic to the source position, to its polarization or to path effects from the propagation along the topography. Subsequently, we investigate the seismic signature of a rockfall impact. For this, an event consisting of a single boulder is selected in order to be able to well separate between different impacts. The synthetic waveforms from a model with flat surface and from the model with topography are compared to characteristics of the real rockfall signals. In order to compare signal amplitudes, impact forces are estimated based on Hertz contact theory (Hertz, 1882).

2 Study site

The study site is located on Piton de la Fournaise volcano, La Réunion, presented in Fgure 1 i) and ii). Its summit is characterized by 340 m deep Dolomieu crater which collapsed in 2007 (e.g. Staudacher et al., 2009). Since then, due to instabilities of the crater walls, high rates of rockfall events are observed within the crater (Hibert et al., 2011; Hibert, Mangeney, et al., 2014; Hibert et al., 2017; Durand et al., 2018; Derrien et al., 2019).

The high quantity of events together with a dense seismic network monitored by the *Observatoire Volcanologique du Piton de La Fournaise* (OVPF) provide excellent conditions for the study of rockfalls. Using recorded seismic signals, past studies investigate the link between rockfall activity and external forcings such as rain or seismicity, the spatio-temporal evolution of rockfall occurrences as well as their volumes (Hibert, Ekström, & Stark, 2014; Hibert et al., 2017; Durand et al., 2018). Additional to the seismic stations, three cameras positioned on the crater rim are continuously monitoring rockfall activity. This allows to correlate video images and rockfall seismic signals.

As an example, Figure 1 iii)-v) show images and seismic signals of a rockfall on the southern crater wall on February 28, 2016. The rockfall consists of mainly three boulders which can clearly be traced on the video. They are moving from the top of the crater wall towards the crater bottom for around 30 s.

The first movement can be detected in snapshot a). At that time, a large signal amplitude is recorded on station DSO, which is located very close to the source position. Subsequently, the rockfall travels through a small valley (see b)) and accelerates towards the position in c). The acceleration of the boulder results in strong impacts which can be detected on both the signal and the spectrogram after time c) at all stations. At the time corresponding to snapshot d), the first boulder arrives at the crater bottom, whereas a second boulder is half-way down. Again strong amplitudes are measured around time d), probably corresponding to the second boulder. Around time e), the last movements of a third block is visible. Afterwards, residual granular activity distributed on the flank is detectable with the video. Signal amplitudes are decaying accordingly.

It can be observed that station DSO records very strong signals in the beginning, while signal amplitudes increase slowly at the other stations. This is certainly related to the changing source-receiver distance. Additionally, as shown hereafter, topography may influence the signal amplitudes depending on the source position in respect to the receiver position. From the spectrograms we can see that the main frequency content is between 3 Hz and 20 Hz. Later we will discuss the frequency content of single impacts using Hertz contact theory. This suggests that the high frequency content is limited by the inverse of the impact time which fundamentally depends on the impact speed.

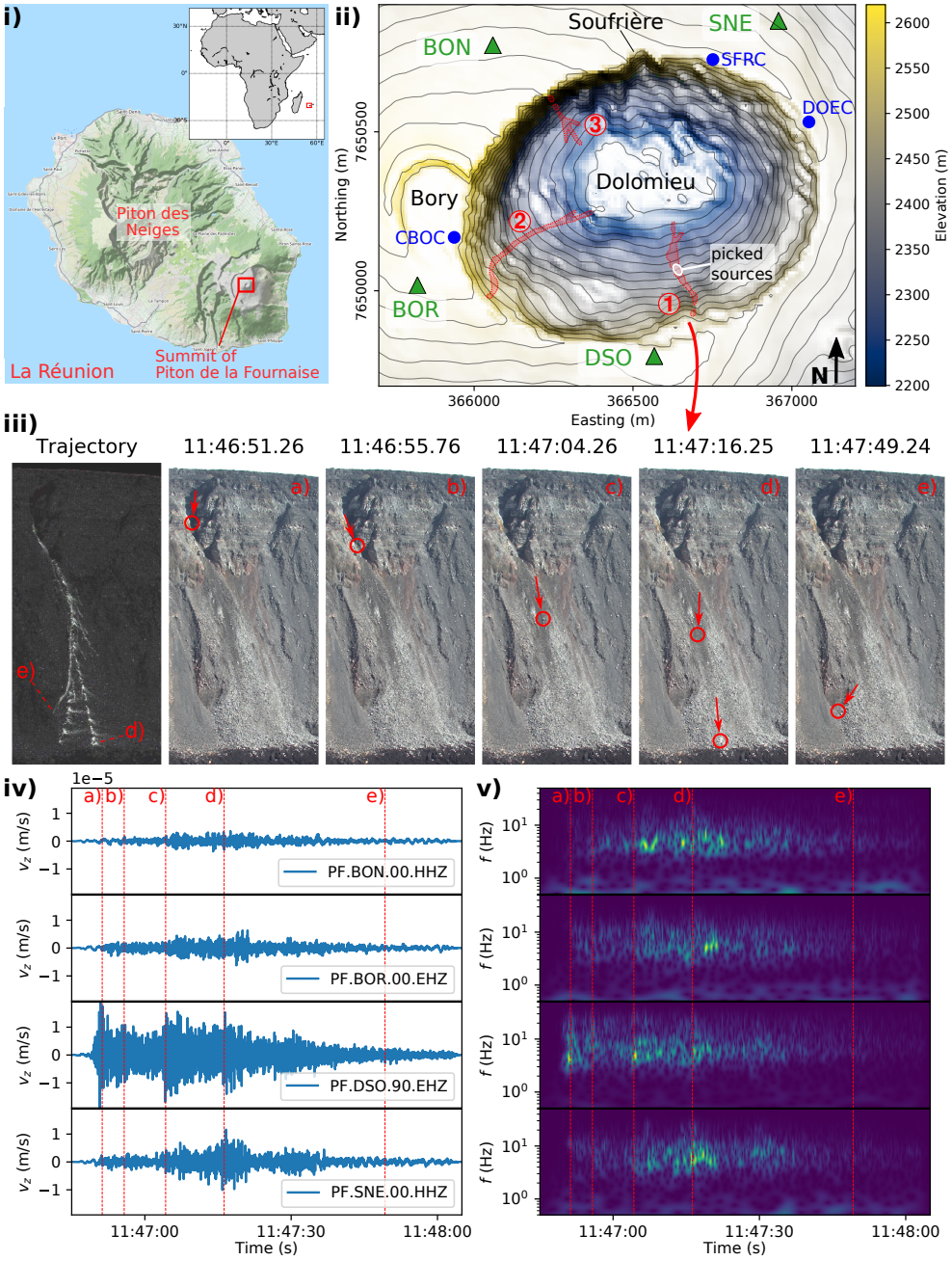

Figure 1. **i)** Map of La Réunion Island with dormant volcano Piton des Neiges and active volcano Piton de la Fournaise. **ii)** The summit of Piton de la Fournaise with 340 m deep Dolomieu crater and smaller craters Bory and Soufrière. Trajectories of three rockfalls which will be analyzed in the following are approximated by red shaded zones. Seismic stations BON, BOR, DSO and SNE are marked by green triangles, cameras CBOC, DOEC and SFRC by blue dots. Contour lines show elevation differences of 20 m. **iii)** Trajectory and snapshots from camera SFRC of rockfall **1** at the southern crater wall on February 28, 2016. Circles and arrows mark a selection of boulder positions and their direction of arrival. **iv)** Vertical ground velocity recorded at all four stations. Vertical lines from a) to e) mark the times of camera snapshots above. **v)** Corresponding spectrograms calculated using Stockwell transform.

3 SEM simulations

In order to study the effect of topography on rockfall seismic signals recorded at different stations, the seismic wave propagation is simulated with the 3D Spectral Element Method (SEM, e.g. Festa & Vilotte, 2005; Chaljub et al., 2007). The seismic source is implemented as a point force of defined direction at the surface of the domain in form of a Ricker wavelet with dominant frequency of 7 Hz. This source covers the bandwidth between 2 Hz and 20 Hz which is predominantly observed for rockfalls at Dolomieu crater.

3.1 Mesh of the Earth model

Figure 2 a) shows a cross-section through the spectral-element mesh. The dimensions of the domain measure $x = 2100$ m (easting), $y = 1800$ m (northing), and $z = 600$ m (depth). Absorbing boundaries (PMLs) of 160 m thickness are added on the sides and on the bottom in order to simulate an open domain. The elements are successively deformed in vertical direction to accommodate the surface topography which is taken from a digital elevation model (DEM) of 10 m resolution. In the following we will first use a filtered topography with 30 m corner wavelength, implemented on a mesh with elements of 20 m side length and afterwards the unfiltered topography on a mesh with elements of 10 m side length which corresponds to the best available DEM. For the latter, in order to decrease computational costs, the element size is increased from 10 m to 30 m at 150 m below the surface as shown in Figure 2 a) (*Zone of refinement*). However, problems in the numerical method can arise when the mesh refinement is distorted by small-scale topography variations. For this reason a low-pass filtered topography is introduced as buffer layer 100 m below the surface in order to dampen strong mesh distortions.

3.2 Velocity model

Three different velocity models are implemented: (1) a homogeneous model, (2) a model with shallow low S-wave velocity layer, and (3) a model with smoothly increasing velocity as proposed by Lesage et al. (2018) for shallow volcano structures. The velocity-depth profiles are illustrated in Figure 2 b) and summarized in Table 1. The generic model by Lesage et al. (2018) is based upon measurements at multiple andesitic and basaltic volcanoes. Wave speed c for P- and S-wave is expressed as follows:

$$c_i(z) = c_{i0}[(z + a_i)^{\alpha_i} - a_i^{\alpha_i} + 1], \quad i = P, S, \tag{1}$$

where z is the depth below surface, c_{i0} are the velocities at zero depth, while α_i and a_i are fitting parameters as defined in Table 1.

The velocity profiles are compared to the S-wave velocity model inverted from ambient noise recordings at Piton de la Fournaise by Mordret et al. (2015). The orange shaded zone shown in Figure 2 b) corresponds to depth-profiles extracted from the inverted 3D model in the vicinity of Dolomieu crater. A good agreement is observed with the Lesage generic velocity profile. The discrepancy in the first 100 m can be associated to missing high frequency content in the model of Mordret et al. (2015), who inverted frequencies below 2.5 Hz.

In order to further validate the Lesage generic model for our study site, Rayleigh velocity dispersion curves from noise measurements at an antenna located around station BON are compared in Figure 2 c) with theoretical dispersion curves of the Lesage generic model. Picks from the antenna measurements are determined using the Modified Spatial Autocorrelation (MSPAC) Toolbox (Köhler et al., 2007; Wathelet et al., 2008) as implemented in the Geopsy software (www.geopsy.org). Theoretical dispersion curves are calculated from the Lesage generic model using modal summation from *Computer Programs in Seismology* (Herrmann, 2013). The measured values are in good agreement with the fundamental Rayleigh velocity dispersion curve. No coherent dispersion curves could not be picked above 6 Hz which is related to the minimum antenna aperture of 30 m.

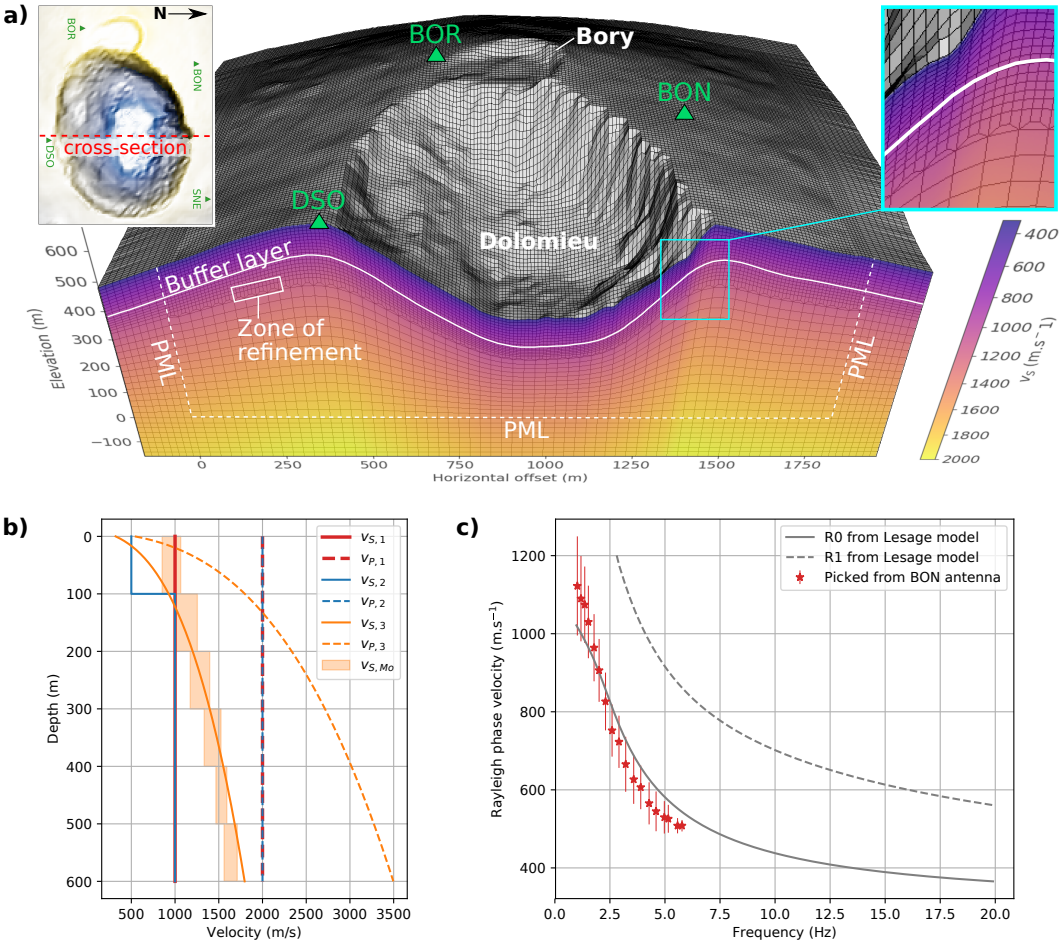

Figure 2. **a)** Cross-section of SEM mesh through Dolomieu crater with topography resolution of 10 m. Perspective as seen from the East with Bory crater located in the background. The color map corresponds to the Lesage generic velocity model (see section 3.2). The buffer layer 100 m below the surface dampens small-scale topography variations. The zone of refinement at 150 m below the surface connects elements of 10 m and 30 m side length. 160 m wide PML boundaries are attached on the sides and on the bottom of the domain. **b)** S- and P-wave velocity depth profiles for (1) homogeneous model ($v_{S,1}$ and $v_{P,1}$), (2) model with shallow S-wave velocity layer ($v_{S,2}$ and $v_{P,2}$), and (3) Lesage generic velocity model ($v_{S,3}$ and $v_{P,3}$). The shaded zone ($v_{S,Mo}$) is extracted from the inverted 3D S-wave model of Mordret et al. (2015). **c)** Theoretical dispersion curves of Lesage generic model for fundamental (R0) and first mode (R1) Rayleigh wave velocity together with picked dispersion curves from antenna around station BON. The errors are estimated from the uncertainty during dispersion curve picking.

Despite missing measurements above 6 Hz, the Lesage generic model is assumed to be the most reasonable model for the shallow high frequency velocity structure of Piton de la Fournaise volcano as it is based upon measurements at comparable volcanoes.

Implementation of the velocity model on the SEM mesh is realized so that it follows the topography elevation. In other words, we define $z = 0$ m at each point on the surface topography. This is reasonable as a main cause for velocity variation is the compaction of material with depth due to increasing overburden pressure. The resulting model is visualized in Figure 2 a) for the case of the Lesage generic velocity profile.

Table 1. Model parameters for the SEM simulations[a]

Model	v_P	v_S	ρ (kg.m^{-3})	Q_P	Q_S
1) homogeneous	2000 m.s^{-1}	1000 m.s^{-1}	2000	80	50
2) low v_S layer	2000 m.s^{-1}	500 m.s^{-1} (top 100 m) 1000 m.s^{-1} (below 100 m)	2000	80	50
3) generic	$c_{P0} = 540$ m.s^{-1} $\alpha_P = 0.315$ $a_P = 10$	$c_{S0} = 320$ m.s^{-1} $\alpha_S = 0.300$ $a_S = 15$	2000	80	50

[a]P- and S-wave velocity v_P and v_S, density ρ, and P- and S-wave quality factor Q_P and Q_S for (1) homogeneous model, (2) model with shallow S-wave velocity layer, and (3) Lesage generic velocity model.

Using a polynomial degree of 5 in the SEM simulations (i.e. 6 GLL points per element), the minimum seismic wavelength must not exceed the element side length. The mesh constructed of 10 m and 30 m elements was confirmed to achieve convergence for the 20 Hz maximum frequency content of the Ricker wavelet and $v_S \geq 320$m.s^{-1} minimum velocity (the numerical time stepping is defined in accordance to the CFL condition).

Rock density ρ as well as quality factors Q_P and Q_S for intrinsic attenuation of P- and S-wave velocity, respectively, are chosen based on previous studies on Piton de la Fournaise and similar volcanoes (Battaglia & Aki, 2003; O'Brien & Bean, 2009; Hibert et al., 2011). All parameters are summarized in Table 1.

3.3 Topography resolution

In the following we investigate the influence of topography resolution on the simulated wave propagation from the model with Lesage generic velocity profile. A vertical point force of 7 Hz Ricker source-time function is placed on the southern crater wall, corresponding approximately to the starting position of the rockfall shown in Figure 1 iii). Figure 3 a) compares synthetic seismograms of vertical component obtained from a model with flat surface, from a model with 20 m topography resolution (low-pass filtered with 30 m corner wavelength), and from a model with 10 m topography resolution. Waveforms recorded at the crater surrounding stations BON, BOR, DSO and SNE are shown.

First of all we can observe that the amplitude diminishes on the models with topography in respect to the simulations from the flat model. Further, topography causes waveforms of longer duration and of more complex forms. For the flat model, wave packets corresponding to body waves, 1st mode Rayleigh waves and fundamental mode Rayleigh waves are well separated. They become less distinguishable when introducing topography. However, it is noticeable that the first part of the wave train is almost identical for both models with topography. At later times, amplitudes are smaller on the model with 10 m topography resolution. This suggests, that mainly fundamental Rayleigh waves are affected as well as 1st mode Rayleigh waves of higher frequencies which arrive later due to their lower velocity compared to low frequencies of the 1st mode. Body waves may stay unaffected as they interact less with topography and the recording stations are located at relatively flat planes.

Figure 3 b) shows spectra of the signals recorded at station BON. Differences between the two models with topography become evident above around 5 Hz. This corresponds to a minimum wavelength of 116 m for the fundamental Rayleigh wave ($\lambda \approx 580$ m.s$^{-1} \div$

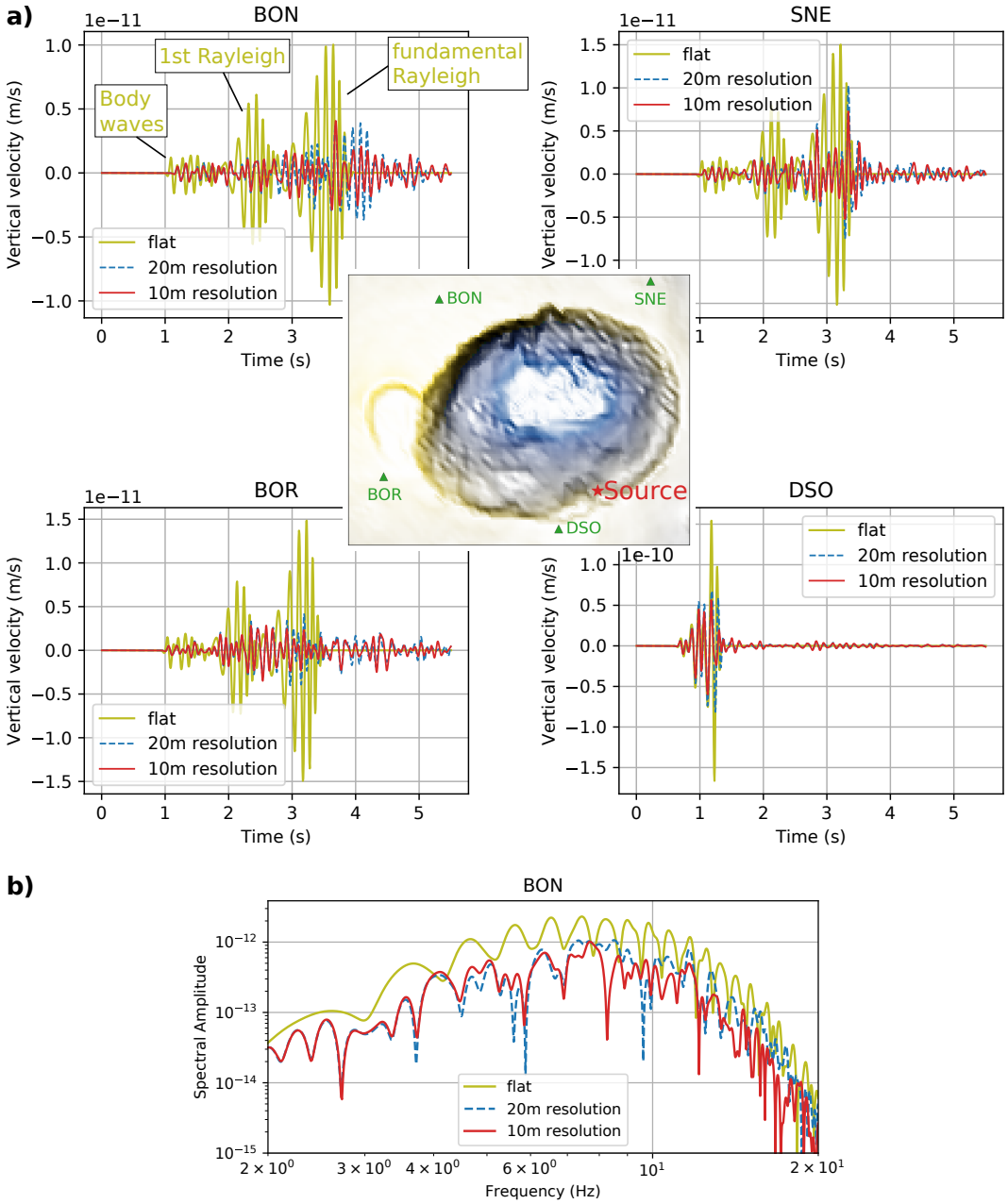

Figure 3. Influence of topography resolution on synthetic seismograms from Lesage generic velocity model. **a)** Comparison of synthetic seismograms (vertical velocity) from model with flat surface, model with 20 m topography resolution and model with 10 m topography resolution. Seismograms recorded at stations BON, BOR, DSO and SNE which are surrounding Dolomieu crater. The source is located on the southwestern crater wall. **b)** Corresponding spectra recorded at station BON.

5 Hz ≈ 116 m). Concluding that wavelength below 116 m are still sensitive to the change in topography resolution, it means that 1st mode Rayleigh waves of above 7 Hz are affected ($\lambda \approx 800\,\mathrm{m.s^{-1}} \div 7\,\mathrm{Hz} \approx 114\,\mathrm{m}$). This analysis suggests surface waves are sensitive to changes in topography resolution which are 5 times smaller than their wavelength.

The decrease of the amplitude at all stations for the higher resolved topography suggests that more energy is scattered along the surface during the propagation. Interestingly, S. J. Lee, Chan, et al. (2009) finds the opposite when comparing waveforms on different topography resolution for a source deep beneath the surface. This implies that the source position plays a major role for the effect of topography. On the one hand, topography can increase ground shaking and thus trap energy close to the surface. On the other hand, in the case of waves traveling along the surface, the topography can increase scattering and thus prevent energy to propagate. Similar conclusions are drawn by S. J. Lee, Komatitsch, et al. (2009) who investigate how topography effects are modulated by the source depth in regards to ground motion in a basin located behind a mountain range.

3.4 Wave propagation from a vertical surface load

We now visualize the wave field at different time steps in order to better understand the wave propagation along the topography. This is done for all three velocity models to show the interaction of subsurface geology and surface topography. For comparison, all simulations are carried out on the domain with 20 m elements (with topography filtered at 30 m corner wavelength) which is computationally less expensive. Again, a vertical point source is placed on the southern crater wall. Figure 4 shows synthetic seismograms recorded on the surface along an array crossing the source position, Dolomieu crater and station BON (see inset for location of the array). Snapshots of the propagating seismic wave field on a cross-section along the array are shown below. All amplitudes correspond to vertical ground velocity. In order to enhance visibility of the wave field over time, the simulations here are realized without intrinsic attenuation unlike for all subsequent analyses.

For the simulation with the homogeneous domain (left column of Fig. 4), we can identify in the first snapshot at time $t = 0.8$ s the P-wave traveling downwards as being the fastest wave with propagation direction parallel to the shown vertical ground velocity. At time $t = 1.6$ s the original S-wave is visible on the bottom of the cross-section. The S-wave can be identified as the direction of propagation is perpendicular to the vertical ground velocity. Just above is a newly created S-wave (annotated as SR) which separated at the bottom of the crater from the Rayleigh wave due to the convex topography. Yet, part of the energy continues as Rayleigh wave along the topography towards the rim of the crater. Also visible is a diffracted surface wave (annotated as Rd). It split from a wave front traveling towards station BOR and took a curved path along the flank of the crater. At time $t = 2.0$ s we can see this diffracted Rayleigh wave continuing outside the crater and arriving at station BON at different azimuth than the Rayleigh wave which traveled diagonally across the crater and its rim (annotated as Rf). The energy of Rayleigh wave Rf was partly reflected at the crater rim so that a new Rayleigh wave Rr is traveling backwards through the crater. Up front (on the very right of the domain), a direct S-wave hits the surface and is partly reflected and converted to build a straight P-wave front traveling downwards at an oblique angle to the horizontal (annotated as SP).

Adding a low S-wave velocity layer (middle column in Fig. 4) drastically changes the wave field due to reflections within this layer and the dispersive character of Rayleigh waves. Looking at the synthetic seismograms we can observe in the first 2.5 s a wave train of dispersive character overlaid by multiples. Compared to the homogeneous model, it is of increased complexity and longer duration due to internal reflections within the low velocity layer. At around $t = 2.6$ s the waves hit the crater rim opposite to the source and are partly reflected just as in the homogeneous case. The snapshots at times $t = 2.6$ s and $t = 3.8$ s show in contrast to the homogeneous case a much more scattered wave field of irregular amplitude patterns. Similar to S. J. Lee, Chan, et al. (2009) who find characteristic patterns dependent on the resolution of the imposed topography, the characteristic length of these patterns is likely to be related to the resolution of the topography and the flat element surfaces of 20 m side length.

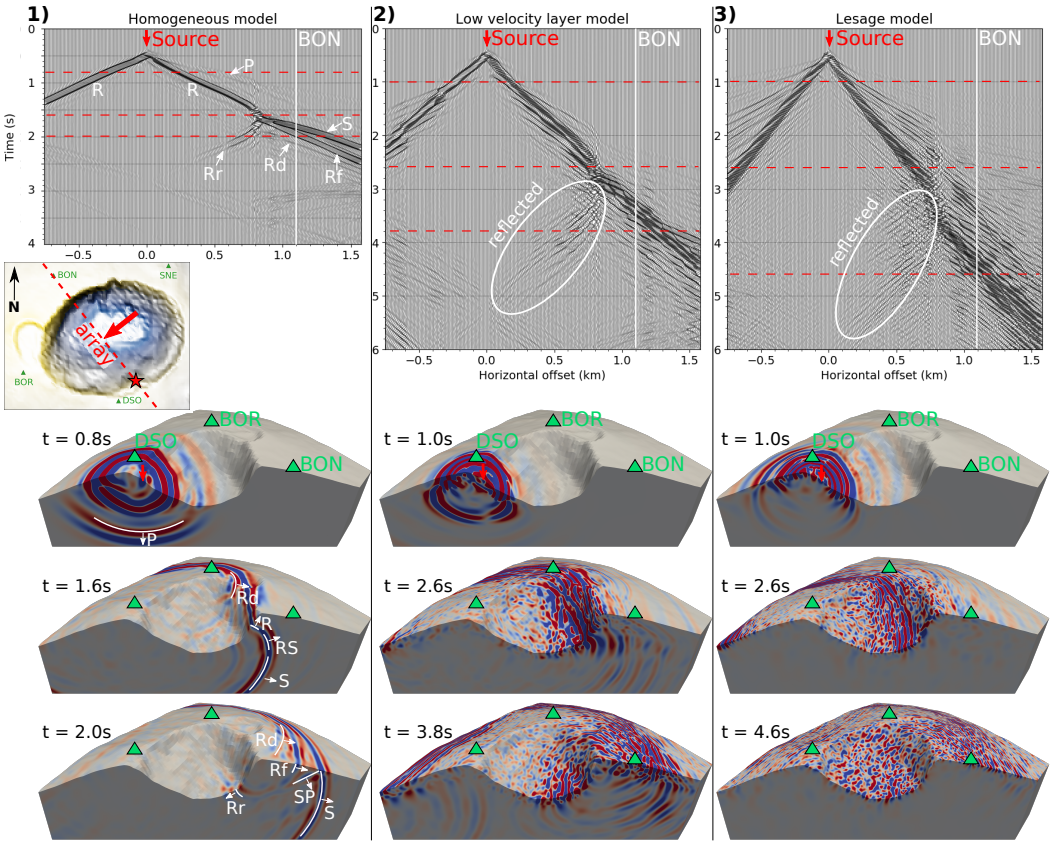

Figure 4. Wave propagation from a vertical surface load on different velocity models. Synthetic seismograms (*top row*) recorded at an array crossing the source, Dolomieu crater and station BON (see inset) for (1) homogeneous model (*left*), (2) model with shallow S-wave velocity layer (*middle*), and (3) Lesage generic velocity model (*right*). Traces are normalized to themselves and show vertical ground velocity. Snapshots of the wave field on cross-sections along the same array are shown below, corresponding to the times marked by red dashed lines. Annotations denote P-wave (P), S-wave (S), P to S converted wave (PS), Rayleigh to S converted wave (RS), Rayleigh wave (R), reflected Rayleigh wave (Rr), diffracted Rayleigh wave (Rd), and diagonally traveled Rayleigh wave (Rf). Note that intrinsic attenuation was not applied in these models in order to enhance visibility of the propagation wave field. This caused reflections from the boundary on the left at later times.

In the case of Lesage generic velocity model (right column of Fig. 4) the majority of energy stays close to the surface of the domain due to the velocity gradient. Scattering of the wave field along the topography is even more elevated than in the case with low velocity layer and the duration of shaking is prolonged. From synthetic seismograms (top right of Fig. 4) we can still identify the outward propagation of energy as well as the reflection of part of the energy at the crater rim.

After having observed the simulated wave propagation qualitatively, we will now quantify the influence of topography. For this, we compare simulations from models with and without topography, taking intrinsic attenuation into account.

4 Influence of topography on simulated wave propagation

Seismic amplitudes carry crucial information of the seismic source and can be used to infer source locations and acting forces. However, as can be concluded from the simulated wave propagation above, topography together with the underlying geology can strongly influence ground motion. Consequently, the measured amplitudes have to be interpreted according to both source properties (including the resulting radiation patterns) and propagation effects. In the following, topography induced amplification is quantified as a function of different velocity models and different source polarizations. This can be helpful to better interpret the spatial distribution of amplitudes and eventually account for amplified signals.

4.1 Amplification from vertical source

In order to quantify topographic ground motion amplification, simulations on a model with topography are compared to a reference model with flat surface. The comparison is performed for both vertical peak ground velocity PGV_z and total kinetic energy E. Quantifying PGV amplification is important when interpreting signal amplitudes. However, it does not measure the increased complexity and duration of recorded waveforms caused by scattering and diffraction of the wave field along the topography. These effects can be incorporated by calculating energy amplification. Also, frequency dependencies are not considered. For this reason we will later look at different frequency bands or take spectral ratios when analysing observed rockfall signals.

To quantify vertical PGV amplification, the maximum vertical ground velocity is measured at each point on the surface defined on a grid with 30 m spacing. The top row of Figure 5 shows the peak ground velocity ratios $\mathrm{PGV}_{z,T}/\mathrm{PGV}_{z,F}$ between model with topography and flat reference model for the three velocity models.

The total kinetic energy is proportional to the measured squared ground velocity $\vec{v}$ integrated over the total signal duration d:

$$E_i \propto \int_d \left(v_{x,i}^2(t) + v_{y,i}^2(t) + v_{z,i}^2(t)\right)\,\mathrm{d}t, \tag{2}$$

with $i = T, F$ for the model with topography and the flat reference model, respectively. Multiplication with mass density ρ is necessary to calculate the true kinetic energy. In order to quantify topographic induced energy amplification in respect to the flat reference model, the ratio E_T/E_F is calculated at each grid point. In this case, the dependency on the mass density vanishes as its value is identical for the two models. The resulting energy amplification is shown on the bottom of Figure 5 for the three different velocity models.

4.1.1 PGV amplification

Analyzing PGV amplification shown on the top of Figure 5, the homogeneous model shows a contrast between source side of the crater and the opposite side: on the source side an amplification of PGV is present while the far side is characterized by a strong deamplification. The amplification on the source side (+12% at DSO) can be explained by the simultaneous arrival of surface and direct waves emitted from the source. Deamplification on the far-side of the source (−83% at BON and −87% at SNE) can be understood as shadow zone behind the crater as a major part of wave energy is diverted downwards into the subsurface due to the crater shape.

In case of the model with low velocity layer, general amplification on the source side and deamplification on the far-source side of the crater are still present but contrasts are less pronounced (deamplification at station SNE goes down to −67%) and patterns become more complex (DSO is now deamplified by −19%). The introduction of a low velocity layer causes more energy to stay at the surface and thus reduces the shadow zone behind the crater. The uneven topography together with the underlying low velocity layer

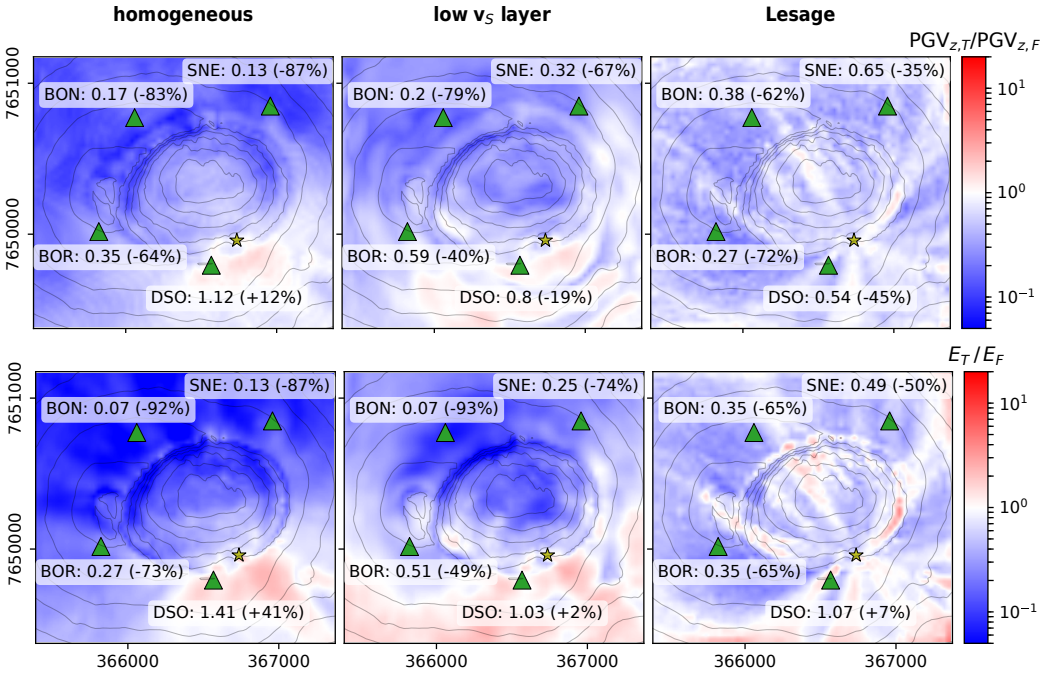

Figure 5. Topographic amplification from a vertical point force. Amplification for vertical PGV (*top*) and total kinetic energy (*bottom*) is calculated in respect to a flat reference model for the homogeneous model (*left*), the model with shallow low velocity layer (*middle*) and the Lesage generic velocity model (*right*). The yellow star illustrates the source position and green triangles mark station locations. Annotations give ratios measured at the station locations as well as percentage of topographic amplification. Neighboring contour lines differ 60 m in elevation.

causes complicated reflections and wave conversions which lead to increased complexity of amplification patterns.

The contrast between source side and far-source side of the crater decreases further for the Lesage generic velocity model (−45% at DSO, −62% at BON and −35% at SNE). As could be seen on the wave propagation snapshots in Figure 4, the gradient causes energy to stay close to the surface. Whereas a lot of energy is lost downwards due to the crater topography in the homogeneous model as well as in the low velocity layer model, the velocity gradient in the Lesage generic model guides waves efficiently along the crater topography or back to the surface which causes a more homogeneous amplification pattern. Scattering away from the surface due to surface roughness as well as conversion from vertical to horizontal energy leads to an overall deamplification in vertical PGV. Still, due to focusing mechanisms of the 3D topography, ray-shaped zones of PGV amplification can be observed originating at the source. The amplification patterns will presumably change with the location of the source. Related to this we show later that spectral ratios of observed rockfall signals are characteristic for the source position.

4.1.2 Energy amplification

As mentioned before, the increased complexity and duration of recorded waveforms due to scattering and diffraction of the wave field along the topography can be incorporated by measuring energy amplification as shown on the bottom of Figure 5.

In general, the amplification patterns of kinetic energy show more contrast than the PGV ratios. This is due to the fact that topography does not only influence peak

amplitude, but also complexity and duration of the signal. For the homogeneous model, amplification increases to +41% at DSO and decreases to −92% at BON. Behavior for the model with low velocity layer is very similar. For the Lesage generic model, the ray-shaped zones of amplification are considerably more pronounced than in case of PGV amplification. Given that horizontal ground velocity is considered when computing the kinetic energy, this observation suggests that topography guides both vertical and horizontal energy along the same paths. Remarkable as well is increased amplification at parts of the crater cliff ridge which is possibly due to the discussed reflection of Rayleigh waves at these positions.

In order to verify that the amplification pattern differences between the velocity models do not solely arise from changes in wavelength, amplification patterns in different frequency bands are compared in Appendix A. Figure A1 shows energy amplification in three different frequency bands for the homogeneous model and the Lesage generic model. While the amplified source side and deamplified far-source side remain for all frequency bands on the homogeneous model, we can see complex amplification patterns for all frequency bands on the Lesage generic model. This suggests that the amplification patterns are not only characteristic for a certain wavelength but fundamentally depend on the wave propagation along the surface topography in conjunction with the underlying velocity model.

4.2 Amplification from horizontal source

Up to now only vertical surface loads were considered. However, the basal forces generated by rockfalls on the ground can also have horizontal components. Here we show amplification patterns for a horizontal source on the Lesage generic velocity model. Figure 6 illustrates vertical PGV amplification (*left*) and energy amplification (*right*) for a wave field generated by a horizontal surface force polarized in north-direction.

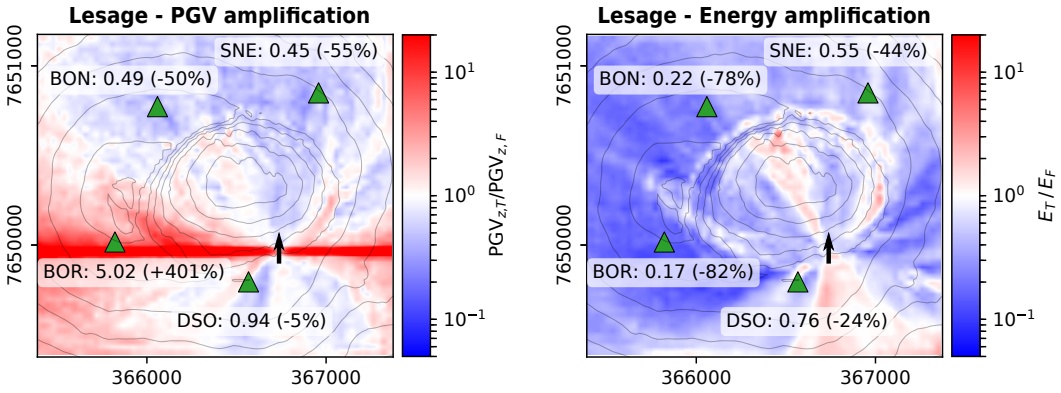

Figure 6. Topographic amplification from a horizontal point force in north-direction. Amplification for vertical PGV (*left*) and total kinetic energy (*right*) is calculated in respect to a flat reference model for the model with Lesage generic velocity profile. The black arrow illustrates the source position and its polarization. Green triangles mark station locations. Annotations give ratios measured at the station locations as well as percentage of topographic amplification. Neighboring contour lines differ 60 m in elevation.

A strong directionality is visible in the PGV amplification pattern. This is due to the fact that in case of the flat reference model a horizontal source does not generate vertical seismic energy perpendicular to its polarization. Topography however can change this by conversion from transverse energy or due to diffracted waves paths.

The directionality patterns are no longer visible when analyzing the amplification of total kinetic energy. This is because all components of the measured ground velocity are considered in the energy calculation. It is remarkable that the energy amplification pattern is similar to the one from the vertical source as shown before in Figure 5. This suggests that topography guides seismic energy on trajectories along the surface dominantly dependent on the source position rather than the source polarization. We will come back to this hypothesis later when studying inter-station spectral ratios of real rockfall signals.

4.3 Surface roughness and crater geometry

The amplification patterns observed in the previous section are characterized by complex spatial distributions. We will now perform tests on domains with synthesized surface topographies in order to better understand the contributions of certain geometric features to the amplification pattern. More concretely, we will study a planar surface with natural roughness as well as synthetic crater shapes of different depths and curvatures. Surface roughness and crater dimensions are defined in resemblance of our study site on Piton de la Fournaise volcano. The starting domain is a cube of size 2360 m × 2360 m×600 m, meshed by elements of 20 m side length. The subsurface medium of all domains corresponds to the Lesage generic velocity model. As above, a 7 Hz Ricker wavelet is used as surface point force.

The domain with planar rough surface is constructed from an area of the DEM at Piton de la Fournaise volcano and band-pass filtered at corner wavelengths of 40 m and 100 m. This way, minimum and maximum wavelengths of the fundamental Rayleigh wave on the Lesage generic model are below and above the range of topography wavelengths, respectively (i.e. $\lambda_{15\,\mathrm{Hz}} \approx 390\,\mathrm{m.s^{-1}} \div 15\,\mathrm{Hz} = 26\,\mathrm{m}$ and $\lambda_{5\,\mathrm{Hz}} \approx 580\,\mathrm{m.s^{-1}} \div 5\,\mathrm{Hz} = 116\,\mathrm{m}$). The resulting domain is shown in Figure B1 **a)**. For the synthetic crater geometry, we use the equation for crater topographies proposed by Soontiens et al. (2013). However, using a smooth, symmetric crater shape results in symmetric interferences as illustrated in Figure B1 **a)**. In order to avoid these artificial amplification patterns of perfect symmetry, the above defined surface roughness is added to the elevation values of the synthetic crater shape, leading to the model shown in Figure B1 **c)**.

Figure 7 **a)** compares synthetic seismograms recorded along arrays on the domains with flat surface, with planar rough surface and with crater topography. From the model with the flat domain, we can identify dispersive Rayleigh waves of fundamental and 1$^{\mathrm{st}}$ mode as well as body waves. Introducing surface roughness leads to strong scattering and hence prolonged ground shaking. The two Rayleigh modes are no longer clearly separated, even though the propagation of the main energy from the fundamental mode can be identified. Introducing the crater topography adds more complexity. The wave field becomes distorted in particularly close the crater walls. This is similar as for the real crater topography before (see Fig. 4).

We now investigate the effect of the surface topographies at different frequency bands. For this, we quantify similar as before the amplification of total kinetic energy in respect to the flat reference model. Note that we here present energy instead of PGV as the first accounts for both amplitudes and prolonged ground shaking and hence gives a more general picture. Figure 7 **b)** shows energy amplification on both the rough planar domain and the domain with synthetic crater in frequency bands of 3-7 Hz and 13-17 Hz.

It is observable that both frequency bands are influenced by the rough planar surface. Recall that the rough topography is band pass filtered at corner wavelengths 40 m and 100 m and that minimum and maximum wavelengths of fundamental Rayleigh waves are below and above the range of topography wavelengths, respectively. We remark ray-shaped zones of amplification which are blurred in the lower frequency band and become sharper towards higher frequencies, related to the shorter interfering wavelengths. The variation of topography seem to guide energy along this ray paths. In contrast, some areas of pronounced topography variation (visible by the densification of contour lines) seem

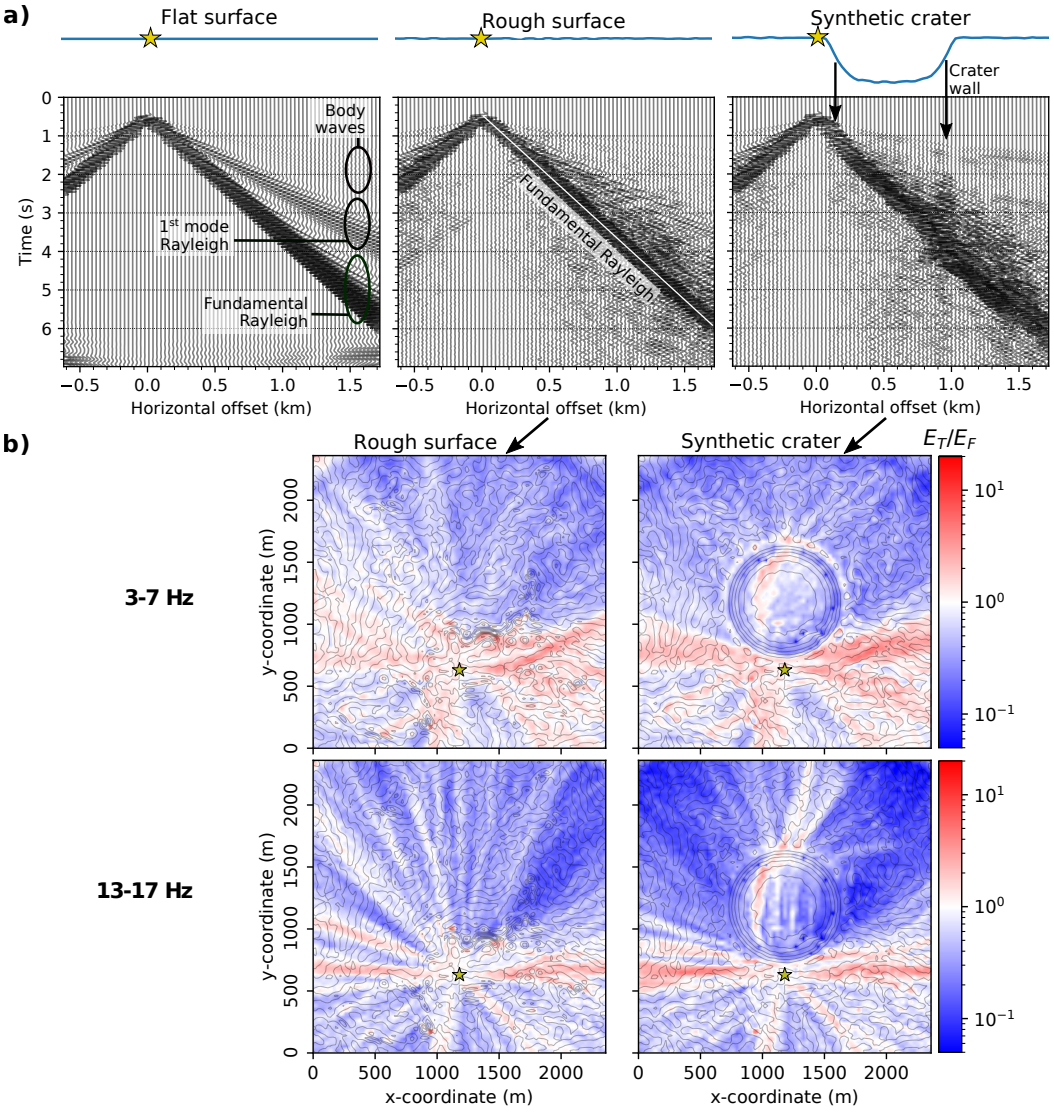

Figure 7. **a)** Synthetic seismograms of vertical ground velocity from models with flat surface (*left*), rough planar surface (*middle*), and synthetic crater shape (*right*). Seismograms are normalized to themselves and recorded along the surface profiles which are illustrated by blue lines above. The yellow star marks the position of the vertical source. Note that the spurious reverberations in case of the flat surface model after the signal (> 6 s) are trimmed for the analyses hereafter. **b)** Energy amplification in different frequency bands for model with rough surface (*left*) and with synthetic crater (*right*). Energy amplification in respect to the flat reference model in frequency bands 3-7 Hz and 13-17 Hz.

to shield the propagation of energy and cause shadow zone behind them. This can for example be observed in north-east direction of the source.

Analysing the energy amplification on the domain with synthetic crater, we can recognize similarities to the amplification patterns to the previously analyzed planar rough surface. This is because the same surface roughness is used whose imprint is now superimposed on the amplification caused by the crater topography. Globally, the wave field is deamplified behind the crater (as seen from the source position). Higher frequencies

seem to be more affected by this than lower frequencies. Nonetheless, even at high frequencies, paths of amplified energy can traverse the crater which might be associated to waves which travel on both sides around the crater and interfere opposite to the source. This effect is very pronounced in the case of a smooth and perfectly symmetric crater topography as illustrated in Fig. B1 **a)** and can also be observed from the simulations on the models with real topography of Dolomieu crater (compare to Fig. 5).

We further study the effect of amplification on different crater depths and curvatures. The crater parameters were chosen so that on the one hand crater depth varies from small to big with fixed curvature and on the other hand curvature varies from weak to strong with fixed crater depth. The resulting profiles and their curvatures are compared to a profile through Dolomieu crater on the left hand side of Figure 8.

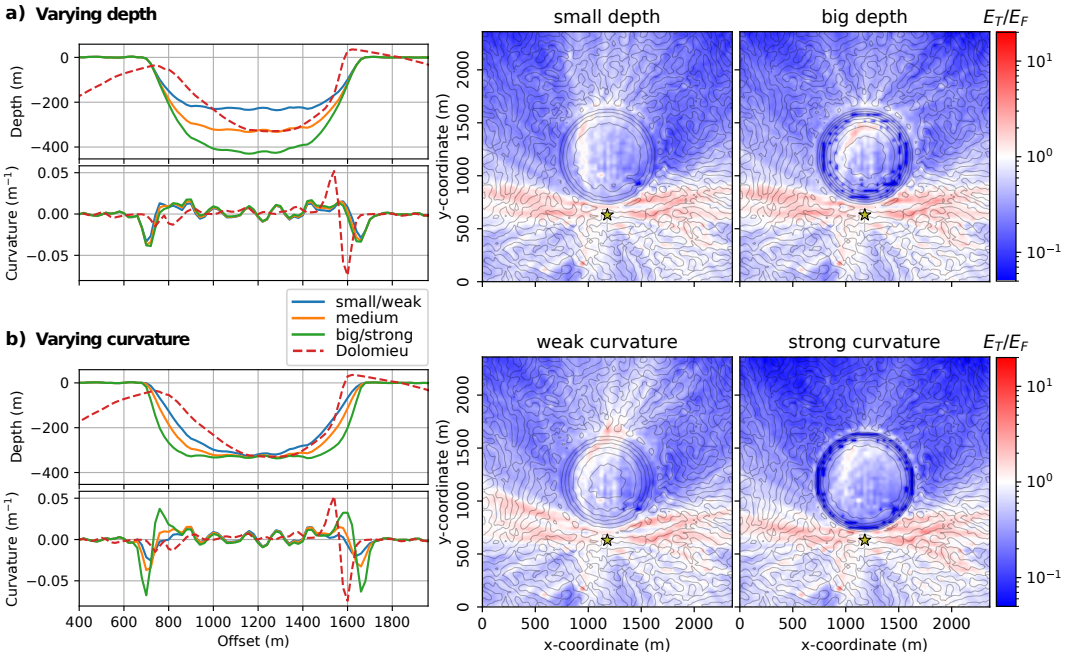

Figure 8. *Left:* Profiles through the synthetic crater topographies. **a)** crater depths vary from small to big with fixed curvature and **b)** curvatures vary from weak to strong with fixed crater depth. Red dashed lines correspond to a profile trough Dolomieu crater and its corresponding curvature. *Right:* Comparison of energy amplification from crater geometries of smallest and biggest depths as well as of weakest and strongest curvature. Contour lines mark elevation differences of 50 m and the yellow star denotes the source. Note that spurious blue dots inside the crater (especially at steep flanks in case of big depth) were caused by numerical measurement problems at these positions.

The energy ratios from the simulations on the domains with synthetic crater shapes are shown on the right hand side of Figure 8 for the whole frequency range. Comparing amplification patterns from varying crater depth and curvature, it seems that the curvature has a stronger influence on the ground motion. Going from small depth to big depth in Figure 8 a), the amplification pattern just varies slightly. The biggest change is observed behind the crater directly opposite to the source. Amplification is decreasing at this point with increasing crater depth. In contrast, inside the crater an increase of amplification can be detected. This changes of amplification patterns might be related to interferences caused by the symmetric crater form. On the other hand, going from weak to strong curvature in Figure 8 b), the shadow zone behind the crater is strongly increas-

ing. This is not only true directly opposite to the source position but also diagonally across the crater. This suggests that the increased crater curvature is shielding off more energy by reflecting or deflecting the wave field sideways or into downwards into the subsurface.

The analyses suggest that the variations of curvature have stronger effects on ground motion than variations of crater depth. It is important to note that the wave field is influenced by topography features of scales both below and above the seismic wavelength. This was observed from the experiments with planar rough surface as well as with the synthetic crater whose dimensions ($\sim$ 800 m diameter, $\sim$ 300 m depth) largely exceed the seismic wavelengths.

The experiments on the synthetic model surfaces allowed us to explore effects from individual aspects of the topography on the wave field. The insights can be transferred to our study side at Piton de la Fournaise volcano as the scales are deliberately chosen similar. Having said this, it must be concluded that the overall effect on the wave field is governed by the whole configuration and cannot be reduced to an individual feature (as e.g. only small-scale versus only big-scale topographic variations). Simultaneously, the source position plays a defining role. In particular for the here studied surface sources, topography related amplitude modifications at a given station can only be predicted if the source position is known.

5 Seismic signals from rockfalls at Dolomieu crater

We will now study observed seismic signals generated by rockfalls at Dolomieu crater. As the influence of the topography changes with the source position, we analyze the signals at specific times corresponding to specific rockfall positions. First we will investigate spectral ratios between stations of time windowed rockfall signals. The objective is to clarify as to whether simulations can reproduce the observed spectral ratios when taking into account topography. Subsequently we will focus on a single block impact, identifying its seismic signature and comparing observed and simulated amplitudes by estimating the generated impact force using Hertz contact theory.

5.1 Observed spectral ratios between stations

For the analysis we select three rockfalls with similar trajectories on the southern crater wall corresponding to rockfall location **1** in Figure 1 ii). Trajectories of the rockfalls were identified from camera recordings. Snapshots of the three events are shown in Figure 9 together with an image of the whole trajectory reconstructed from differences of successive snapshots. Below, the corresponding seismic signals recorded at stations BON, BOR, DSO and SNE are presented.

Station DSO shows the strongest amplitudes, especially in the beginning of the rockfall. This is due to the fact that the three rockfalls are starting very close to this station. BON contains the smallest amplitudes, being the furthest station and on the opposite side of the crater. The dynamics of the three events is not entirely identical. Event 1) consists of a single boulder bouncing down towards the bottom of the crater while some more blocks are following with a time lag of around 15 s. In contrast, event 2) has two blocks moving down closely following each other with a time lag of only 4 s as can be seen on snapshot 2b). Event 3) consists of a main boulder with a smaller block following much later with a lag of about 50 s.

Despite these differences, we compare spectral ratios between stations in time windows R1, R2 and R3 during which the main blocks are moving within identical areas. The spectral ratios are computed from the measurements at stations BOR, DSO (only vertical component) and SNE with respect to station BON (note that BON is selected as reference stations as it turns out it is the least affected by local site effects). In order to avoid spurious fluctuations, the spectra are smoothed following Konno and Ohmachi (1998) before calculating the ratios. The obtained curves are shown as dark blue lines (TW-R1, -R2, -R3) in Figure 10 for vertical- (*top*), north- (*middle*) and east- (*bottom*)

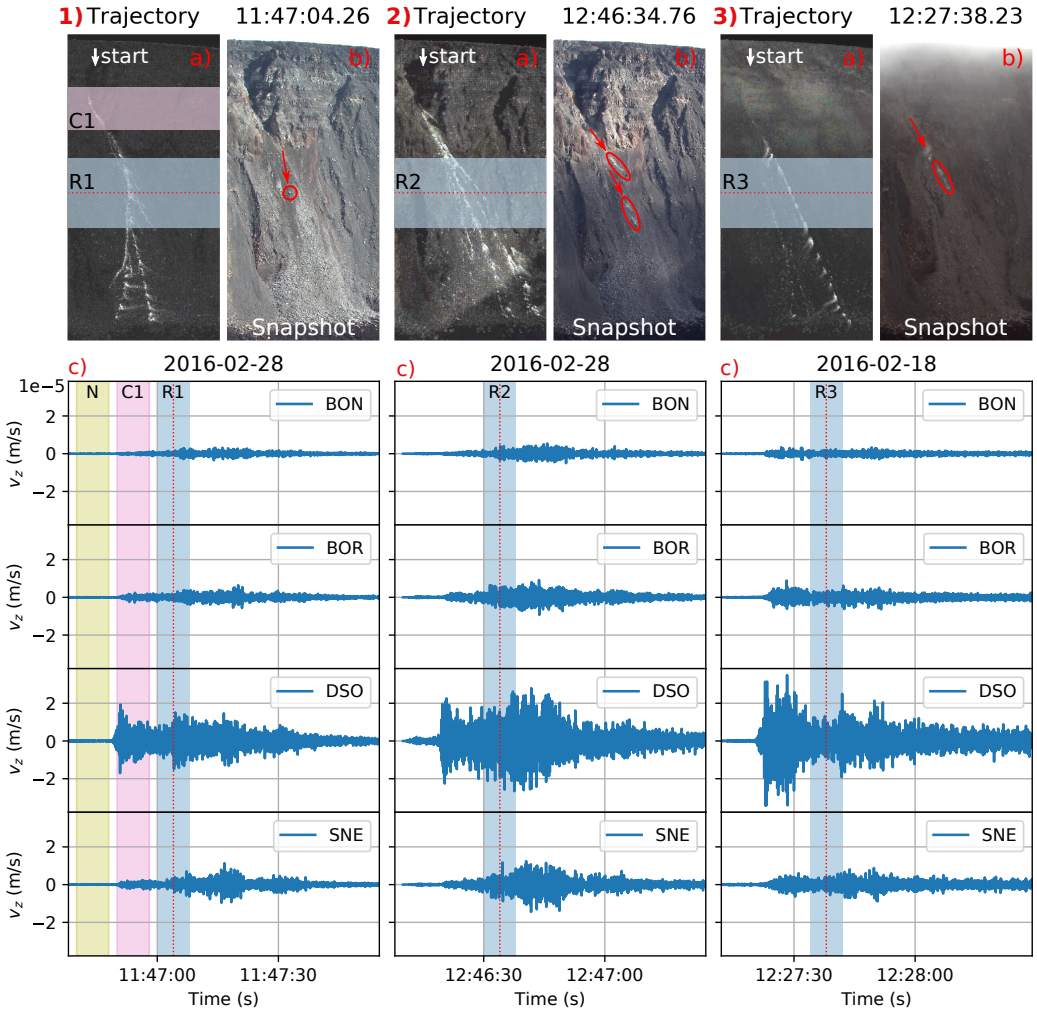

Figure 9. Three similar rockfalls on the southern wall of Dolomieu crater, corresponding to rockfall location **1** in Figure 1 ii). The events occurred on 1) February 28, 2016 at around 11:47, 2) February 28, 2016 at around 12:46, and 3) February 18, 2016 at around 12:27. Panel a) shows the total trajectory of each event (seen from camera SFRC). The approximate starting positions at top of the crater wall are indicated by white arrows. Panel b) shows snapshots (seen from camera SFRC) at a chosen time for which all three rockfalls are at comparable positions. Panel c) presents the rockfall seismic signals, on which the red dotted lines mark the time of the snapshots. Time windows R1, R2, and R3 (blue shaded zones) are defined ±4 s around these times. The corresponding location of these time windows are also indicated as blue shaded zones on the trajectories. Same holds for reference time window C1 (magenta shaded zone), which corresponds to the beginning of event 1). Noise time window N is taken from recordings before event 1).

components. It is visible that the spectral ratios behave similarly for each of the events and for each component.

In order to verify that the spectral values are indeed characteristic to the rockfall signals at the chosen positions, the curves are compared to ratios from noise recordings (TW-N), ratios from beginning of event 1) (TW-C1), and ratios from a rockfall occuring at a different position in the crater (TW-C2), corresponding to trajectory **2** in Figure 1 ii). It can be observed that the spectral curves from noise recordings as well as from

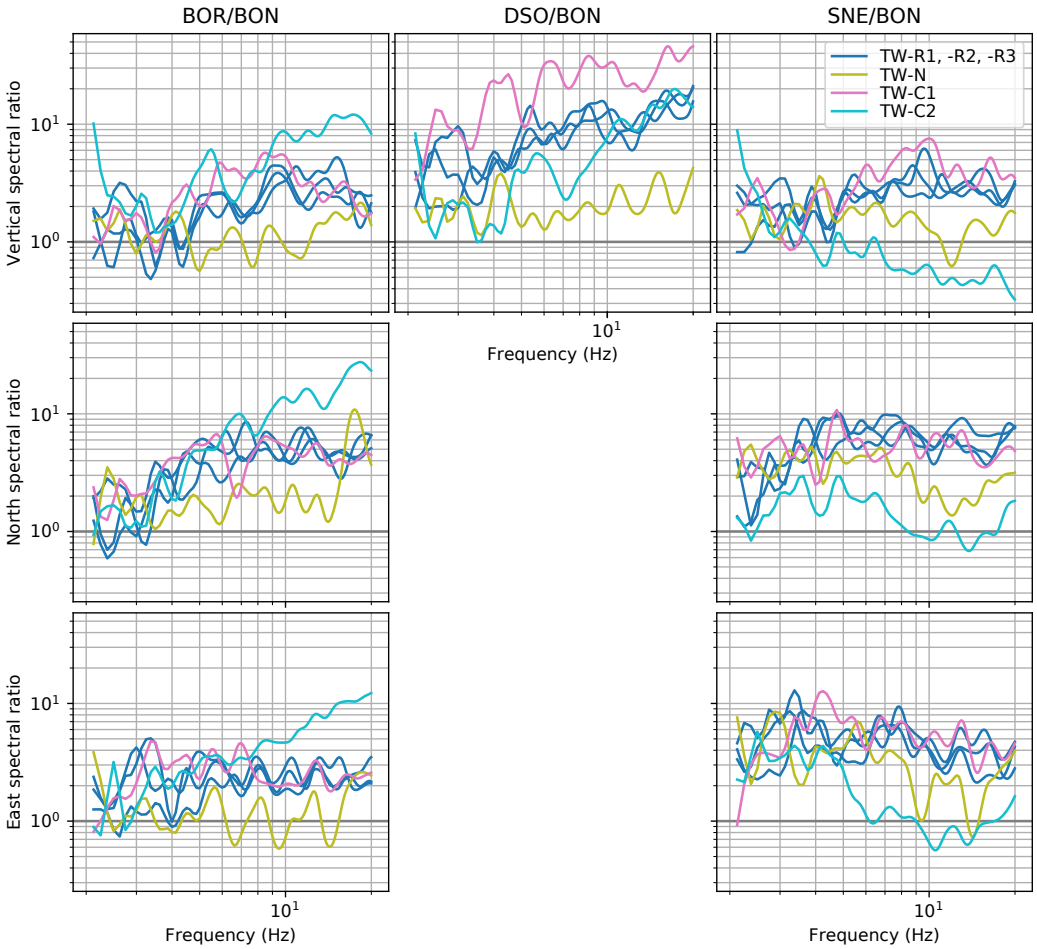

Figure 10. Spectral ratios from rockfall seismic signals recorded at stations BOR (3 components), DSO (1 component) and SNE (3 components) in respect to station BON for vertical- (*top*), north- (*middle*) and east- (*bottom*) components. Time windows TW-R1, -R2, and -R3 correspond to rockfalls 1), 2), and 3) as defined in Figure 9. Time windows TW-N and TW-C1 correspond to noise recordings and beginning of rockfall 1), respectively. Time window TW-C2 is taken from a rockfall on the southwestern crater wall, corresponding to rockfall location **2** in Figure 1 ii).

the rockfall in the southwest show strong deviations from curves R1, R2 and R3. In Appendix D spectral ratios of the rockfall in the southwest are compared to two further events in the same location. This again results in similar curves for all three rockfalls in this area.

The spectral curves C1 from the beginning of event 1) are quite similar to curves R1, R2 and R3 for ratio BOR/BON and SNE/BON. This can be explained by the comparable source-receiver distances. Nevertheless, discrepancies are detectable at certain frequencies. On the other hand, strong deviations are present for ratio DSO/BON. This is because the source position shifts strongly respectively to station DSO.

The findings suggest that the spectral ratios are characteristic for the position of the rockfall seismic source. The source-receiver distance is one factor which leads to this result. Hereafter we will investigate as to whether the source-receiver distance alone can explain the spectral ratios or if they are better reproduced when topography is considered in the simulations. Further, different radiation patterns are produced when chang-

ing the direction of the source. For this reason we additionally study the influence of the source direction on the spectral ratios.

5.2 Comparison of observed and simulated spectral ratios

The seismic source of a rockfall can be very complex as multiple impacts of different magnitude can occur simultaneously at different positions. Hence, it is very difficult to correctly simulate the rockfall seismic signal, especially at high frequencies. For this reason, spectral ratios between stations are very convenient in order to compare real and synthetic signals. By this, the signature of the source is removed from the signal and solely propagation path effects are left. Nevertheless, we have to keep in mind two points when comparing observed and simulated spectral ratios.

Firstly, local subsurface heterogeneities can modify recorded amplitudes and thus influence inter-station ratios. These geological site effects are not considered in the simulations. Therefore, in order to enhance comparability between the observed and simulated spectral ratios, the recorded signals are corrected using site amplification factors estimated from volcano-tectonic (VT) signals. The spectral amplification curves are calculated and discussed in Appendix C where we also show a comparison between simulated to uncorrected observed spectral ratios. The observed inter-station ratios hereafter have been corrected by deconvolution of the recorded signals with the corresponding amplification factors.

Secondly, different source polarizations cause different radiation patterns. This is illustrated in Figure 11 a), where a force on a flat surface is polarized in vertical and in horizontal direction, respectively. If the radiation pattern is not radial symmetric, which is only the case for vertical ground motion from a vertical source, the spectral ratios are affected depending on the azimuthal position of the respective receivers. The direction of a rockfall seismic source depends both on the rockfall dynamics and on the underlying slope. The generated forces from a boulder impact are schematically illustrated in Figure 11 b). The resulting force F_r is composed of a force F_n normal to the slope and a force F_t tangential to the slope which depends on the slope angle, the direction of movement and the friction between the moving mass and the ground.

In order to analyze the influence of the source direction on the spectral ratios, we compare a vertical force to a normal force and a tangential force. Note that we assume that the tangential force is parallel to the slope of steepest descent. To consider a spatially distributed source in the simulations, the mean spectral ratio is calculated from a selection of multiple sources. This allows simultaneously to evaluate the sensitivity of the curves on the source positions. Concretely, 7 source positions are picked from a grid of 10 m spacing within the white shaded zone marked in Figure 1 ii). The zone correspond to the region in which rockfalls 1), 2), and 3) are present during time windows R1, R2, and R3, respectively (see Figure 9).

5.2.1 Simulated spectral ratios from model with flat surface

Figure 11 c) compares spectral ratios BOR/BON from the observed signals (site effect corrected) with simulated ratios of differently polarized sources on a model with flat surface. The source directions are determined from the slope of Dolomieu topography at the corresponding position before implementation on the flat domain. For spectral ratios of vertical component (*left*), a tangential force direction results in much smaller values compared to the other sources. As the slope is dipping northwards, the tangential force is orientated in north-direction. Station BOR is located west of the source position which is transverse to the source direction. For this reason, a smaller signal amplitude is measured at station BOR in comparison with station BON (ratio < 1), even though BOR is slightly closer to the source. Nevertheless, the tangential force also contains a vertical component which ensures that the ratio is in the same magnitude as the observed ratios. This is different for the spectral ratios of north component (*middle*), where

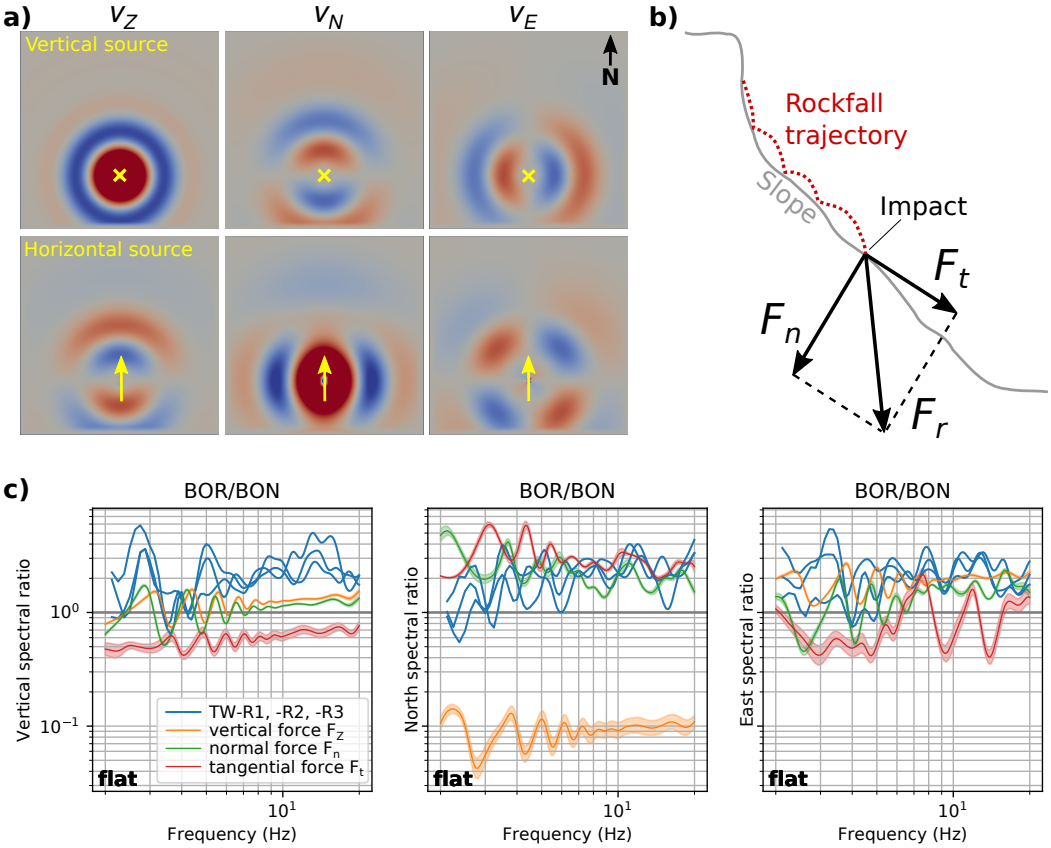

Figure 11. **a)** Seismic radiation patterns from a vertical source (*top*) and from a horizontal force (*bottom*) for ground velocity v_Z, v_N, and v_E of vertical-, north-, and east-component, respectively (red: positive, blue: negative amplitudes). **b)** Forces generated by a rockfall impact. The red dotted line illustrates the trajectory of a bouncing boulder. The impact generates force F_n normal to the slope. Depending on the boulder velocity tangential to the slope and of the friction coefficient μ, a tangential force $F_t = \mu F_n$ is generated (assuming Coulomb friction). Normal and tangential forces add up to resulting force F_r. **c)** Comparison of spectral ratios BOR/BON from real signals TW-R1, -R2, -R3 (as in Fig. 10) and from simulations on the flat domain with varying source direction: vertical force as well as normal and tangential force according to the Dolomieu topography at the corresponding position. Shaded zone of the simulated ratios indicate the standard deviation from the mean value of the 7 picked source positions.

a striking discrepancy of more than a magnitude results from the vertical source. A vertical force does not generate horizontal transverse energy which is why almost no signal is recorded on the north component at the eastwards located station BOR. For the east spectral ratios (*right*), the tangential force shows again the strongest deviation for reasons similar as for the vertical component spectral ratios.

It is evident that the source direction can strongly influence the measured spectral ratios between stations. This is caused by the corresponding radiation pattern and the respective positions of source and stations. In the following we will show that the dependency on the source polarization becomes smaller when the wave propagation is influenced by surface topography.

5.2.2 Simulated spectral ratios from model with topography

Figure 12 shows observed and simulated spectral ratios of vertical-, north-, and east-component for all station pairs after considering the Dolomieu crater topography in the simulations. None of the simulated spectral ratios shows as large discrepancies to the real curves as previously from the model with flat surface, shown in Figure 11 c). Instead, very similar values can be observed comparing the simulations with different source directions, especially towards higher frequencies. This indicates, that the spectral ratios are in this case not dominated by the direction of the source (and the hence produced radiation pattern) but rather by the propagation along the topography.

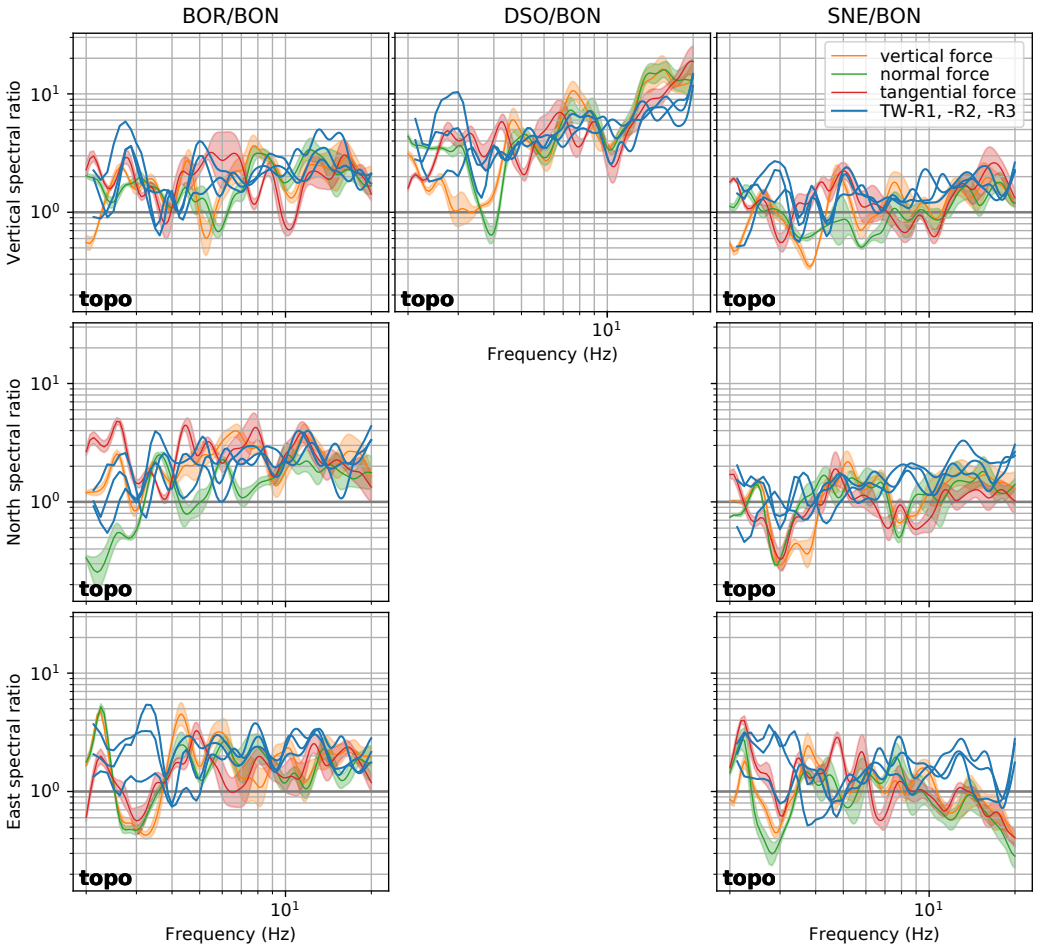

Figure 12. Spectral ratios BOR/BON, DSO/BON and SNE/BON calculated from real signals TW-R1, -R2, -R3 (as in Fig. 10) and from simulations on domain with Dolomieu topography for vertical component (*top*), and horizontal components in north- (*middle*) and east- (*bottom*) direction. Simulations are realized with varying source direction: vertical force, force normal to the slope and force tangential to the slope. Shaded zone of the simulated ratios indicate the standard deviation from the mean value of the 7 picked source positions which are indicated in Figure 1 ii).

Greater deviations between the different source directions can be detected at lower frequencies, such as for example on the north component of ratio BOR/BON below 3 Hz. Assuming fundamental Rayleigh waves, this corresponds to wavelengths above 250 m ($\lambda \approx 750\,\mathrm{m.s^{-1}} \div 3\,\mathrm{Hz}$). With a distance of around 500 m between the source position and

station BOR, it is likely that these low frequency waves have not travelled enough wavelengths in order to be completely dominated by its propagation along the topography.

At higher frequencies, observed and simulated spectral ratios are in better agreement. An exception is the east component of ratio SNE/BON where the simulated values underestimate the observed ones. This might be caused by medium heterogeneities which are not fully accounted for through the correction of the observed signals with the site amplification functions.

Analyzing the sensitivity of the ratios on the source position, generally larger standard deviations (shaded zone of uncertainty around the mean) are present after introducing topography compared to the results from the flat model in Figure 11 c). This means that a slight change of source position allows more variability of the ratios when considering topography and can eventually better explain the observed spectral ratios.

Clearly, the spectral ratios also depend on the relative source-receiver distance. For example, the high values of ratio DSO/BON results from the fact that the source is very close to station DSO. Furthermore, the values increase towards higher frequencies. This is related to the attenuating properties of the medium which cause the amplitudes of higher frequencies to decrease faster with traveled distance than lower frequencies.

The analysis suggests that the spectral ratios are characteristic for the source position and dominated by the propagation along the topography rather than by the radiation patterns which are caused by the source directions. To further validate this hypothesis, the same comparison between observations and simulations is carried out in Appendix D for rockfalls located on the southwestern crater wall.

In the following, rockfall signals are analyzed at each station individually. For this, we will focus on a single rockfall impact, identifying the characteristics of its seismic signal as well as comparing observed and simulated amplitudes with the help of Hertz contact theory.

5.3 Seismic signature of a rockfall impact

We will now analyze in detail the seismic signal generated by single impacts of a rockfall at Dolomieu crater. Signal characteristics are interpreted based on the comparison with synthetics simulated on models with and without topography. The comparison between observed and simulated signal has to be carried out very carefully due to uncertainties of the seismic source and the medium of propagation. It is important to emphasize that we do not want to reproduce the recorded signal but rather understand some of its features as for example arrival times, waveform complexity and amplitudes.

For the analysis, a single boulder rockfall is chosen with well separated impacts which can be tracked on video. These criteria are fulfilled by an event on January 22, 2017, located on the northern crater wall. Figure 13 shows a camera snapshot of the rockfall at time of impact N2 as well as the impact locations and the rockfall seismic signal recorded on the vertical component at the closest station BON. Two boulder impacts, N1 and N2, separated around 4 s from each other, are analyzed hereafter. A minor impact n1 can be detected 1 s after impact N1. It will be used later to estimate the fall velocity of the boulder. Note that the impact times are estimated from the video according to the appearance of small dust clouds which are caused by the impacts. The time delay between true impact and visibility of the dust cloud affects the precision of the impact time. In the same order, the precision is limited by the sampling time of 0.5 s between successive snapshots.

The broadband seismic signal of the rockfall shown in Figure 13 **c)** is characterized by two main lobes. These two main lobes are separated by a gap of low seismic energy at around 10:26:32. During this gap, no impact is detectable on the video. Thus, the boulder is in free fall before hitting the ground at impact location N2. Afterwards, the rockfall splits into several blocks which continue to move downwards on the debris cone of former rockfalls. At these later times it is very difficult to identify single impacts.

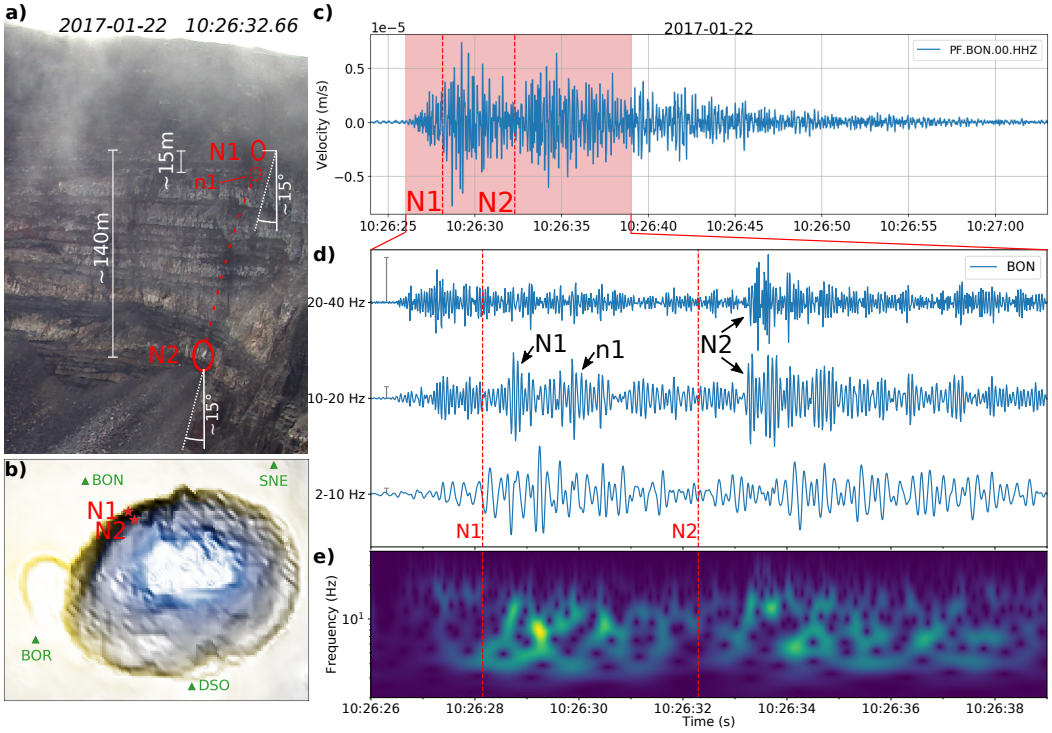

Figure 13. Single boulder rockfall on January 22, 2017. **a)** Camera snapshot taken shortly after impact N2. Estimated vertical distance between impacts and estimated slope angle to the vertical at impact positions. **b)**: Location of impacts N1 and N2 in Dolomieu crater. **c)** Vertical ground velocity recorded at closest station BON in frequency band 2-40 Hz. Red shaded area illustrates the time window of graph below. Dashed lines mark impact times N1 and N2 estimated from video. **d)** Comparison of frequency bands 2-10 Hz, 10-20 Hz, and 20-40 Hz. Signals are normalized to their maximum, gray bars on the left indicate the the relative scaling. **e)** Time-frequency representation of rockfall signal (calculated using the Stockwell transform).

In order to be able to better distinguish single impacts, the seismic signal is filtered in different frequency bands. Figure 13 **d)** compares signals band-pass filtered at 2-10 Hz, 10-20 Hz, and 20-40 Hz. Note that the signals are normalized. Their relative scales can be inferred from the gray bars plotted in the beginning of the signal as well as from the spectrogram below.

The signal filtered in the low frequency band (2-10 Hz) exhibits a smooth amplitude envelope. The two main lobes discussed before can be observed whereas no single pulses can be identified. It contains the strongest amplitudes and thus dominates the broadband signal. Short signal pulses emerge in the high frequency bands. It is evident that seismic sources were already active before impact N1. Unfortunately, these could not be detected on the video. Impacts are possibly hidden behind the clouds on the top of the crater wall. A clear seismic pulse in the frequency range 10-20 Hz can be associated to impact N1. It arrives at the station around 0.5 s after the time determined from the video. A second pulse around 1 s later can be associated to impact n1. It contains slightly smaller amplitudes. The highest frequency band does not show clear corresponding signals to these two impacts. This is different for impact N2. Both high frequency bands show abrupt signal onsets around 1 s after detection time of impact N2 on the video. The following signal can not be described as a single pulse but contains several peaks. This raises the question as to whether the source is made of several impacts or if these peaks result from the seismic wave propagation. Using synthetic seismograms generated

by a point source, we will see hereafter that a single impact can indeed cause such complex waveforms. This in turn means that we cannot simply associate an individual impact to each seismic pulse detected in the signal.

Another interesting observation concerns the impact generated frequencies. As we could see, impact N1 is hardly detectable in the highest frequency range (20-40 Hz), whereas impact N2 produces clear signals in both high frequency bands (10-20 Hz and 20-40 Hz). Arguing with the changing source-receiver distance, we would expect the contrary as N1 is slightly closer to station BON than N2. If we assume that the properties of the boulder and of the underlying ground are identical for both impacts, the change in frequency content must be related to the impact velocity. According to Hertz contact theory, which we will introduce hereafter, higher impact velocities are associated with shorter collision times. The inverse of the collision time constitutes the upper limit of the force spectrum. Hence, as the boulder is accelerating between impact N1 and impact N2, the higher velocity at impact N2 results in a shorter collision time and therefore generates higher frequencies.

5.3.1 Hertz contact theory

In order to predict relative amplitudes of signals generated by impacts N1 and N2, the respective impact forces of the boulder on the ground are estimated. Farin et al. (2015) use the theory of Hertz (1882) to describe the force of an elastic sphere impacting a solid elastic surface. After successfully applying the theory on seismic signals generated during laboratory experiments they analyze real-size rockfall experiments carried out by Dewez et al. (2010). Here we estimate the impact forces in similar fashion, assuming a spherical boulder of radius R and mass m. The maximum impact force F_0 exerted by the sphere perpendicularly to the plane can then be described as

$$F_0 = \frac{4}{3} E R^{1/2}\, \delta_{\max}^{3/2}, \tag{3}$$

where $\delta_{\max}$ is the maximum indentation depth

$$\delta_{\max} = \left(\frac{15 m v_n^2}{16 E R^{1/2}} \right)^{2/5}, \tag{4}$$

with impact speed v_n normal to the plane. E is the effective Young's modulus $1/E^* = (1-\nu_s^2)/E_s + (1-\nu_p^2)/E_p$, where ν_s, ν_p, E_s, and E_p are Poisson's ratio and Young's modulus of sphere and impacted plane, respectively. In the following we discuss the values and uncertainties of impact parameters for N1 and N2, assuming that the boulder and ground properties do not change between the two respective impacts.

First of all, the impact speed v_n normal to the slope is estimated. For both impacts N1 and N2 we assume a sub-vertical fall of the boulder before collision. In other words, the boulder has a vertical speed of v_c at the time of collision. Slope angles at the impact positions are inferred from the DEM to be around $\alpha = 15\,^\circ$. The normal impact speed can then be calculated as $v_n = v_c \sin\alpha$. To estimate v_c for N1 and N2, height differences between the impacts are determined from the DEM using the impact positions estimated from the video. As labeled in Figure 13 **a)**, we find a height difference of around $H_1 = 15\,\mathrm{m}$ between N1 and n1, and a height difference of around $H_2 = 140\,\mathrm{m}$ between N1 and N2. Impacts N1 and n1 are detected 1 s apart from each other. Assuming an approximately constant velocity during this short time window, the vertical speed for impact N1 is $v_{c,1} = 15\,\mathrm{m.s^{-1}}$. For impact N2, acceleration during the long free fall cannot be neglected. The speed is thus derived by $v_{c,2} = v_{c,1} + (2g(H_2 - H_1))^{0.5}$, where $g = 10\,\mathrm{m.s^{-2}}$ is the gravitational acceleration. Hence, a vertical speed $v_{c,2} = 65\,\mathrm{m.s^{-1}}$ is found for impact N2. This leads to normal impact speeds of $v_{n,1} = 4\,\mathrm{m.s^{-1}}$ and $v_{n,1} = 17\,\mathrm{m.s^{-1}}$ for impact N1 and N2, respectively. Considering that the normal impact speed depends on both the boulder speed and the angle between slope and fall trajectory, the error is estimated to be as big as $\pm 50\,\%$.

The boulder size is also approximated using the camera snapshots. The dust cloud caused by impact N2 in Figure 13 **a)** has an estimated length of 5 m. As only the dust clouds and not the boulder itself is traceable on the video, the boulder size is assumed to be less than 1 m. As a perfect sphere is considered in the calculations, the effective radius is roughly estimated to be $R = 0.3\,\mathrm{m}$. Again, we estimate an error on the radius of up to $\pm 50\,\%$. This means that the diameter of the boulder can vary in between 0.3 m and 0.9 m.

A first idea of the boulder mass is given by combining the just estimated radius and the mass density $\rho = 2000\,\mathrm{kg.m^{-3}}$ used in the simulations. This results in a boulder mass of $m = 225\,\mathrm{kg}$. Due to the uncertainties on both boulder shape and density, an error of up to 50 % from 112 kg to 337 kg is expected.

Finally, a typical effective Young's modulus of $E = 10\,\mathrm{MPa}$ is applied following Farin et al. (2015). Again an error of up to $\pm 50\,\%$ is estimated. Having the same relative error of $\pm 50\,\%$, we are able to compare the contribution from each parameter to the total uncertainty of impact force and frequency.

The maximum impact force F_0 can now be calculated using equation 3. This way, we find 84 kN and 485 kN for impact N1 and N2, respectively. These values will be used hereafter to calibrate the seismic source in the numerical simulations. The maximum uncertainty of the impact force is calculated numerically through variation of each parameter by $\pm 50\,\%$. The resulting values are summarized in Table 2, reaching from $-81\,\%$ to $+165\,\%$. Figure 14 **a)** breaks down the contribution of each parameter on the maximum uncertainty. Note that the relative errors are the same for both impacts N1 and N2. We can observe that the variation of impact speed v_n has the greatest effect on the impact force, followed by the boulder mass.

Table 2. Impact parameters[b]

	v_c	α	v_n	$\delta_{\max}$	F_0	T_c	f_c
N1	$15\,\mathrm{m.s^{-1}}$	$15\,^\circ$	$4\,\mathrm{m.s^{-1}}$	0.05 m	$\left(84^{+137}_{-68}\right)$ kN	0.038 s	$\left(26^{+12}_{-10}\right)$ Hz
N2	$65\,\mathrm{m.s^{-1}}$	$15\,^\circ$	$17\,\mathrm{m.s^{-1}}$	0.16 m	$\left(485^{+799}_{-393}\right)$ kN	0.029 s	$\left(35^{+16}_{-13}\right)$ Hz

[b] Parameters of impact N1 and N2: vertical impact speed v_c, angle α between slope and vertical, impact speed v_n normal to the slope, maximum indentation depth $\delta_{\max}$, contact time T_c, and corner frequency f_c.

Concerning the frequency content of the impacts, we analyze the contact duration of the impacts. Following Johnson (1987), the temporal evolution of the Hertzian impact force F_H can be approximated by

$$F_H(t) \approx F_0 \sin(\pi t/T_c)^{3/2}, \quad 0 \le t \le T_c. \tag{5}$$

The force-time function and its frequency spectrum are shown in Figure 15 as a function of impact duration T_c.

We can observe an exponential decay of the spectral amplitude above corner frequency $f_c = 1/T_c$. Johnson (1987) showed, that the impact duration can be approximated by means of maximum indentation depth $\delta_{\max}$ and impact normal speed v_n as

$$T_c \approx 2.94 \frac{\delta_{\max}}{v_n}. \tag{6}$$

Applied to N1 and N2, the impact durations are estimated to be 0.038 s and 0.029 s, respectively. It then follows, using the relation $f_c = 1/T_c$, that the high frequency con-

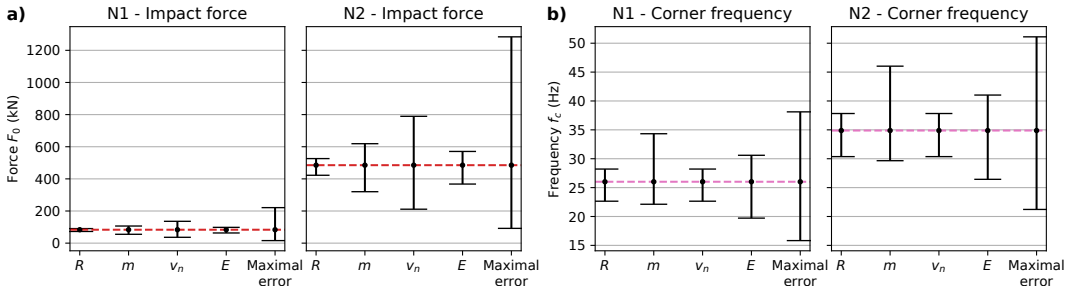

Figure 14. **a)** Uncertainty of impact force F_0 for impact N1 and N2. The uncertainty is calculated numerically through variation of each parameter by ±50 %, i.e. boulder radius R, mass m, normal impact speed v_n and Young's modulus E. Shown are the errors from individual parameter variations as well as the maximal error. Note that the parameter variations lead to identical relative errors for N1 and N2. **b)** Uncertainty of corner frequency f_c for impact N1 and N2 such as in **a)**.

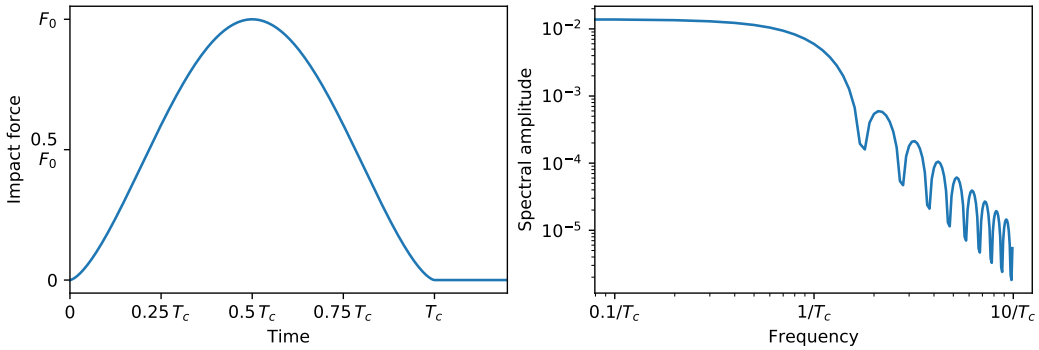

Figure 15. Hertzian impact force and corresponding frequency spectrum. *Left:* Hertzian force-time function F_H normalized by maximum impact force F_0 in dependency of impact duration T_c, which represents the time during which the two bodies are in contact. *Right:* Frequency spectrum of the force-time function. The inverse impact time $1/T_c$ is related to the corner frequency f_c after which the spectral amplitude decays exponentially.

tent of the impacts are limited by corner frequency 26 Hz and 35 Hz, respectively. Table 2 gives an overview over they results together with the uncertainties on the frequency content which was calculated numerically as for the impact force. The maximum uncertainty ranges from −39 % to +47 %. The contribution from each parameter is visualized in Figure 14 **b)** for impact N1 and N2. In contrast to the impact force, the frequency content is least sensitive to normal impact speed v_n. The biggest contribution is constituted by boulder mass m as well as Young's modulus E.

An important result is that Hertz contact theory predicts a higher frequency content for N2 which is related to the higher impact velocity. This is in agreement to the observed waveforms in Figure 13 **d)**: impact N1 can hardly be detected in the high frequency band (20-40 Hz), whereas impact N2 shows a clear pulse despite the slightly bigger source-receiver distance. The theoretical values correspond well to the observations, predicting frequencies up to 26 Hz for N1 and up to 35 Hz for N2.

5.3.2 Comparison of observed and synthetic waveforms

Previously, we tried to associate pulses in the observed seismic signal to impacts detected on the video by crudely interpreting the signal after the time of impact. We will now use numerical simulations to get insights into travel times and expected waveforms. As mentioned before, the intention is not to reproduce observed waveforms, but rather to understand which signal characteristics can be associated to a single impact.

Observed and synthetic signals are compared in the frequency band of 10-20 Hz, in which we could identify short signal pulses associated to the rockfall impacts. At the same time, 20 Hz constitutes the upper frequency limit of our simulations. In order to ensure comparability, the observed signals are corrected with the site amplification functions calculated in Appendix C and subsequently convolved with the 7 Hz Ricker wavelet used in the simulations. The simulated signals are calibrated with the maximum impact forces for N1 and N2 estimated above from the Hertz theory.

First of all, observed and synthetic seismograms are normalized in order to allow an easier comparison of the waveforms. Figure 16 compares vertical ground velocity recorded at stations BON, BOR, DSO, and SNE with simulations from impacts N1 and N2 on models with flat surface and with Dolomieu topography. Source positions of the two impacts are estimated from the videos, see Figure 13 **b)**. As the exact source polarization of the real impacts are unknown, the variability of synthetic waveforms is shown in dependency of different force directions, namely a vertical force F_z, a force F_n normal to the slope and a force F_t tangential to the slope.

Analyzing the synthetic seismograms, we can observe in general that N1 produces smaller amplitudes in respect to N2. This is due to the estimated impact forces of 84 kN and 485 kN, respectively (see Table 2).

However, while seismograms from the model with flat surface keep approximately the same relative amplitudes between N1 and N2 at all different stations, seismograms from the model with topography show more variability. For example, at station BON, the amplitudes of impact N1 are much bigger from the model with topography than from the flat model. This corresponds better to the real observations, where the maximum amplitude of impact N1 is comparable to the maximum amplitude of impact N2. In contrast, we can observe at station DSO that the signal of impact N1 is very small in respect to the signal of N2 in the case of topography. Again, this corresponds well to the observations. As impact N1 and N2 are located very close to each other, the relative amplitudes on the flat model are mainly determined by the relative impact force. Introducing topography influences both the relative (vertical) source position as well as the propagation path which is why we observe more variation on the relative amplitudes.

From the simulations with flat surface, three wave packets following each impact can be detected, which are well separated from each other on the more distant stations BOR, DSO, and SNE. These three wave packets correspond to body wave, 1^{st} mode Rayleigh wave, and fundamental mode Rayleigh wave (see e.g. Figure 7). The arrival time of the 1^{st} mode Rayleigh wave is in good agreement with the first major pulse after each impact. This suggests that the Lesage generic velocity model represents the shallow subsurface velocity around Dolomieu crater reasonably well. However, on the flat model the amplitude of the 1^{st} mode Rayleigh wave is consistently smaller than the amplitude of the fundamental mode. A corresponding amplitude variation cannot be identified on the real signals. In contrast, simulations on the model with topography generate waveforms of more complexity. This increased complexity corresponds better to the observed signals, even if the waveforms do not fit perfectly. The variation of the force direction modifies the waveforms stronger than in the flat case. Also, waveforms vary strongly from station to station. This is not observed in the flat case, in which the waveforms are very similar on stations at comparable source-receiver distances (i.e. BOR, DSO, and SNE). All in all, we can conclude that a single impact can produce complex waveforms, in particular when topography variations are involved. Consequently, it is generally not possible to deduce from a rockfall seismic signal, if the source consists of a single impact of multiple impacts.

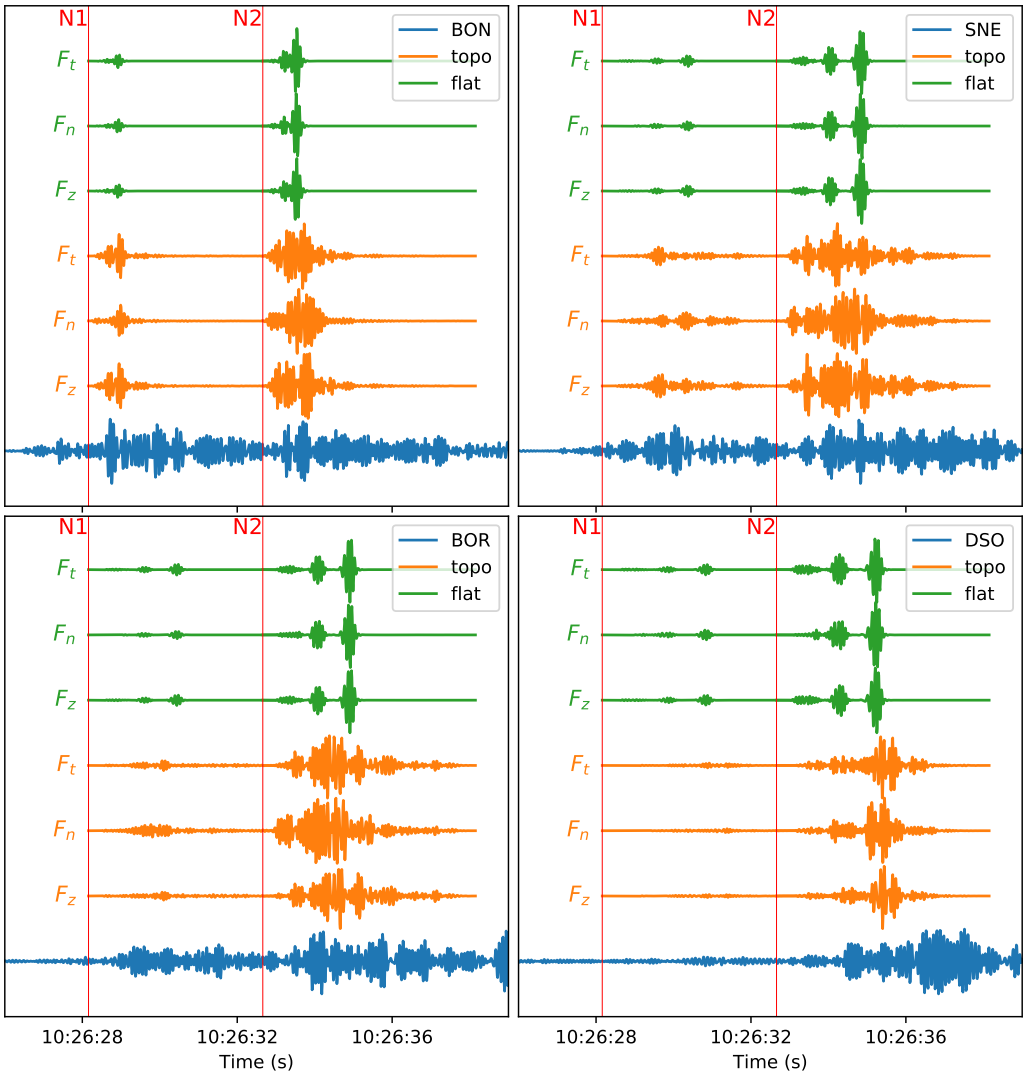

Figure 16. Comparison of rockfall signal with synthetic waveforms from different force directions. Blue lines correspond to vertical ground velocity recorded at different stations for the same time window as shown in Figure 13 **d)**. Red vertical lines indicate impact times N1 and N2 from the video. Synthetic waveforms of impacts N1 and N2 are shown for the model with flat surface (green) and with Dolomieu topography (orange). Source positions are illustrated in Figure 13 **b)**. The variability of waveforms is demonstrated in dependency of a vertical force F_z, a force F_n normal and a force F_t tangential to the slope. All traces are normalized by their maximum.

Complementary to the waveforms, a polarization analysis is carried out which is presented in Appendix E. In the studied frequency range of $10 - 20$ Hz, clear particle motions were only detected at the closest station BON. Here, by slightly changing the source position, we observe that not only propagation effects but also source characteristics have to be considered when interpreting the signal polarization.

Finally, observed and synthetic seismograms are compared without normalization. This way, the absolute signal amplitudes calibrated by the Hertz impact force are evaluated. The total value of the acting force as well as its direction is determined by a vector sum of the force normal and the force tangential to the slope. Tangential force F_t

is inferred from the maximum normal impact force $F_n = F_0$ assuming Coulomb friction $F_t = \mu F_0$, where μ is the material specific friction coefficient. We define $\mu = 0.7$, which is a typical value used for rockfall at Dolomieu crater (e.g. Hibert, Mangeney, et al., 2014). The resulting signal amplitudes for model with flat surface and model with topography are compared in Figure 17 with the observed rockfall signals.

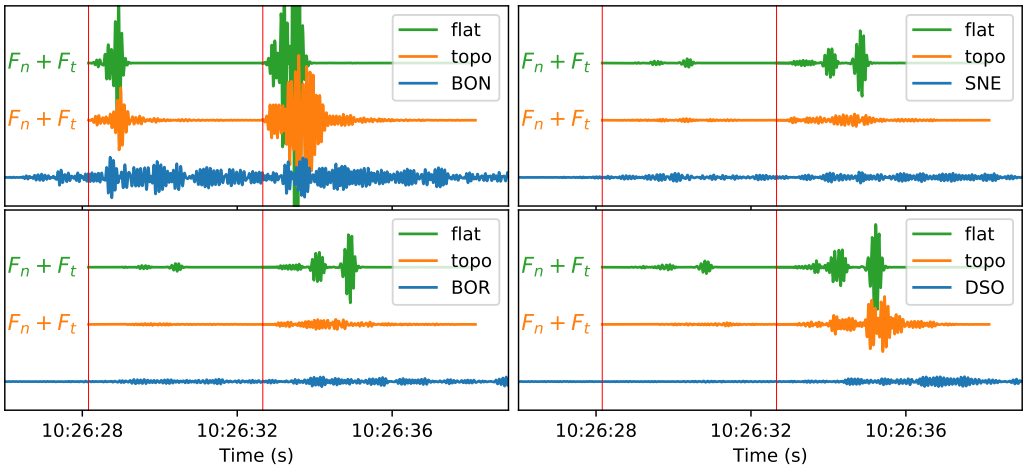

Figure 17. Amplitude comparison between observed and synthetic seismograms. Blue lines correspond to vertical ground velocity recorded at different stations for the same time window as shown in Figure 13 **d)**. Red vertical lines indicate impact times N1 and N2 from the video. Synthetic waveforms of impacts N1 and N2 are shown for the model with flat surface (green) and with Dolomieu topography (orange). The seismic source is constructed by summing force F_n and F_t normal and tangential to the slope. F_n corresponds to the maximum impact force F_0 as shown in Table 2. Source positions are illustrated in Figure 13 **b)**.

We can observe that the simulated and observed amplitudes are of comparable magnitude. Synthetic seismograms from the flat model generally overestimate the observed amplitudes. From simulations on topography, signals of impact N1 are always underestimated, while signals from N2 are overestimated on BON and DSO and underestimated on BOR and SNE. Noteworthy are the relative amplitude changes between the stations. While in the case of the flat model, amplitudes are decreasing with distance from the source, the model with topography breaks this relation. For example, on the flat model the maximum amplitude decreases drastically from station BON to station DSO. In contrast for the model with topography, the signal amplitude of impact N2 is almost half as the one of station BON. This topography induced amplitude change was shown before by means of the amplification maps.

All in all, by employing the Hertz contact theory to calibrate the simulations, we are able to achieve comparable amplitude magnitudes in respect to the observed signals. The observable amplitude deviations can be explained by considering the uncertainties of the derived impact force F_0, which are presented in Table 2 as well as in Figure 14.

6 Conclusion

We investigated the effect of topography on the propagation of wave fields generated by surface point loads. The interplay of topography effect and the underlying velocity model was studied. Given a velocity-depth profile with strong gradient, as proposed by Lesage et al. (2018) for the shallow velocity structure of volcanoes, more seis-

mic energy from a surface source is trapped close to the surface. As a consequence, this leads to more complex spatial distributions of wave field amplification in comparison to a homogeneous model, for which seismic energy can be directed downwards by the topography into the subsurface. Studying the effect of different crater topographies indicates that modifications of the crater curvature affects the wave field stronger than modification of the crater depth.

Simulation were compared with measurement from rockfalls at Dolomieu crater. By analyzing signals generated at specific rockfall locations, it is demonstrated that spectral ratios between stations are characteristic for the source positions. Comparison with simulations further suggests that the spectral ratios are dominated by the propagation along the topography rather than the polarization of the seismic source. This is an important finding with direct implication for the localization of rockfalls. In this context it is important to point out that the influence of the topography on surface waves has to be considered as a propagation effect rather than a local site effect at the recording station. In other words, a surface wave arriving at a recording stations is affected by its total path along the topography. This is similar to body waves which are affected by their total path though the subsurface. Just as body waves are used to infer subsurface properties, the information imprinted on surface waves might be used to infer properties of their origin. In contrast to subsurface properties, surface topography can be measured quite easily and accurately. This allows to accurately simulate the response of topography with numerical models. Nonetheless, the coupling of topographic effects and local site effects from heterogeneities in the subsurface should additionally be considered. In the present study we accounted for local site amplification by estimating amplification factors from VT events. However, it is not granted that surface waves experience the same amplification as a vertical incident wave field. Thus, to better estimate influence of the subsurface, the surface wave propagation has to be modeled including subsurface heterogeneities.

Finally, analyses of the seismic signature from single impacts demonstrate the potential information hidden in rockfall seismic signals. Synthetic waveforms show that a single impact can produce a complex waveform with multiple pulses. While seismograms from the flat model show similar waveforms at all stations, surface topography modulates waveforms as a function of source direction and source position. Also, the relative amplitudes between different stations can strongly be influenced by the topography. Calculations based on the Hertz contact theory suggest that the observed differences in frequency content of the two presented impacts can be explained by differences in impact speeds. For identical boulder and ground parameters, a higher impact speed results in a higher frequency content. Furthermore, amplitudes calibrated by the maximum impact force predicted from the Hertz theory results in magnitudes comparable to the real signals.

The combination of Hertz contact theory and wave propagation simulations is an important step for the interpretation of rockfall seismic signals based on the underlying physical processes. The Hertz impact theory is frequently used to predict the impact force of rockfalls, for example for the design of structural protections (e.g Volkwein et al., 2011). Also, laboratory experiments show the validity of Hertz theory concerning the waves generated by the collision of a ball on a massive plate (e.g. McLaskey & Glaser, 2010). However, only few studies apply the theory to seismic signals from real-scale rockfalls, as done by (Farin et al., 2015; Bachelet et al., 2018). A limiting factor is the complex rockfall source which often consists of multiple simultaneous impacts. For this reason, application to artificially triggered rockfalls which ensures separated impacts of a single boulder would help validate the Hertz theory in the field and to enhance understanding of real impact processes.

Appendix A Energy amplification in different frequency bands

Figure A1 shows energy amplification in three different frequency bands for the homogeneous velocity model (top) and the generic velocity model (bottom). Rayleigh wavelengths on the two models are comparable in frequency band 3-7 Hz for the homogeneous model ($\lambda \approx 1000\,\mathrm{m.s^{-1}} \div 10\,\mathrm{Hz} = 100\,\mathrm{m}$) and in frequency band 8-12 Hz for the Lesage generic model ($\lambda \approx 580\,\mathrm{m.s^{-1}} \div 5\,\mathrm{Hz} \approx 116\,\mathrm{m}$, see dispersion curves in Fig. 2 c)). However, we can observe that the amplification patterns differ from each other in these two frequency bands. This suggests that the respective amplification patterns are not only characteristic of a certain wavelength. The wave propagation essentially depends on the velocity model which hence results in different amplification patterns.

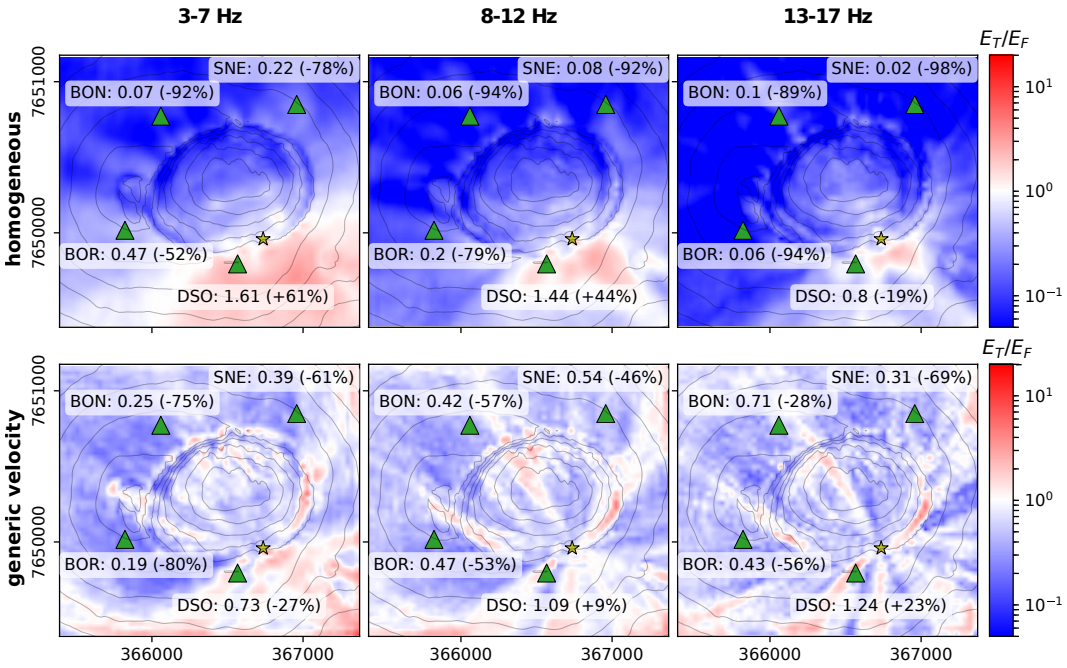

Figure A1. Amplification of total kinetic energy in frequency bands 3-7 Hz (*left*), 8-12 Hz (*middle*) and 13-17 Hz (*right*) for the homogeneous velocity model (*top*) and the Lesage generic velocity model (*bottom*). The yellow star denotes the source, green triangles the stations. Annotations give ratios measured at the station locations as well as percentage of topographic amplification. Neighboring contour lines differ 60 m in elevation.

Appendix B Surface roughness and synthetic crater

Figure B1 **a)** shows the planar domain with added surface roughness which is extracted from a real DEM and band-pass filtered between corner wavelengths of 40 m and 100 m. Figure B1 **b)** demonstrates the symmetric interference patter caused by a perfectly symmetric synthetic crater. Seismic waves are guided on symmetric paths around the crater and interfere constructively on the opposite side of the source where strong amplification is visible. In order to break this symmetry and get a more realistic crater model, the surface roughness is imposed onto the domain with the synthetic crater geometry which can be seen in Figure B1 **c)**.

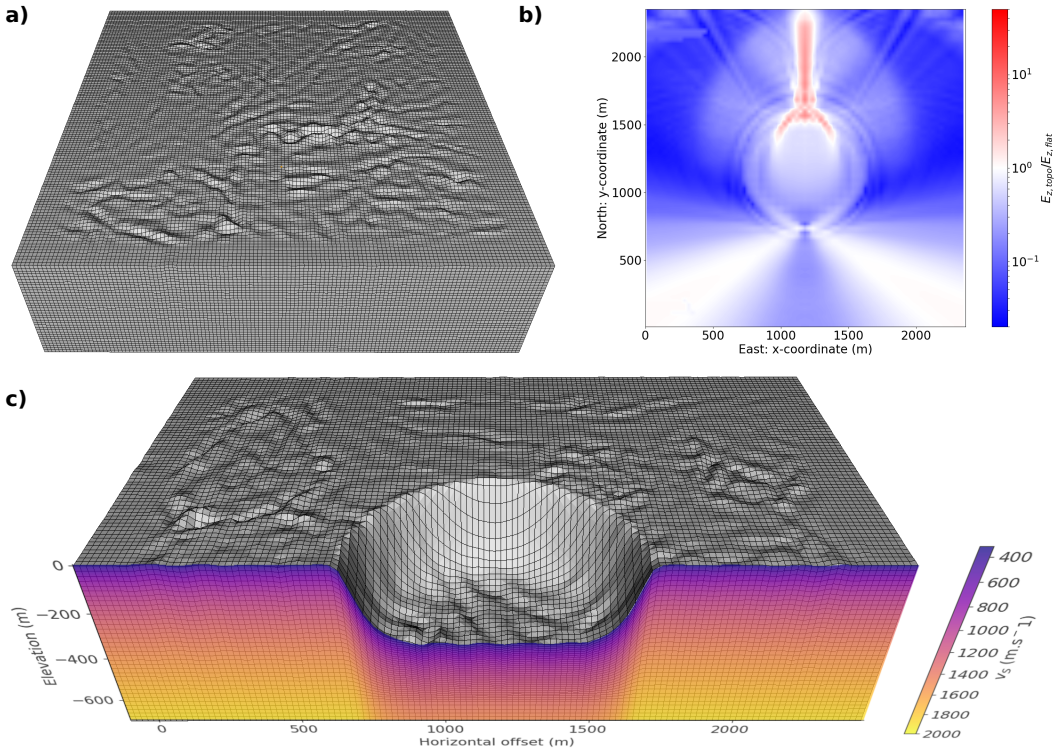

Figure B1. **a)** Model domain with surface roughness of wavelengths between 40 m and 100 m. **b)** Amplification pattern of vertical energy caused by a perfectly symmetric crater shape. In order to avoid the symmetric interference pattern, the surface roughness from **a)** is added to the synthetic crater shape. A cross-section of the resulting domain is shown in **c)**, where the colormap represents the velocity model from the Lesage generic velocity-depth profile.

Appendix C Estimation of site effects caused by local subsurface structures

Before calculating the site amplification functions, Figure C1 compares spectral ratios from the uncorrected rockfall signals and from simulations on the models Dolomieu topography. It can be observed that ratios from the simulations seem to be smaller than the real values. In particular ratio SNE/BON is strongly amplified, especially on the horizontal components. This amplification is possibly caused by local structures in the subsurface which are not accounted for in the simulations. Hereafter, we estimate local site effects in order to correct the recorded signals and ensure comparability between observations and simulations.

Site effects are estimated from seismic signals generated by volcano-tectonic (VT) events which are centered around 2 km below Dolomieu crater. 36 events are selected from a catalog compiled by Duputel et al. (2019). To compute the amplification functions, BON was qualified as adequate reference station based on low spectral amplitudes of both VT signals and noise H/V ratios. The spectral ratios are computed from FFT spectra after applying the smoothing function proposed by Konno and Ohmachi (1998) in order to avoid spurious fluctuations. Figure C2 shows the mean spectral amplification functions and their standard deviation calculated from all VT events for all components.

Strongest amplification is experienced by station SNE with factors up to 7 on its horizontal components. This can explain the strong mismatch between observations and simulations which are visible in Figure C1. Single-component station DSO also seems

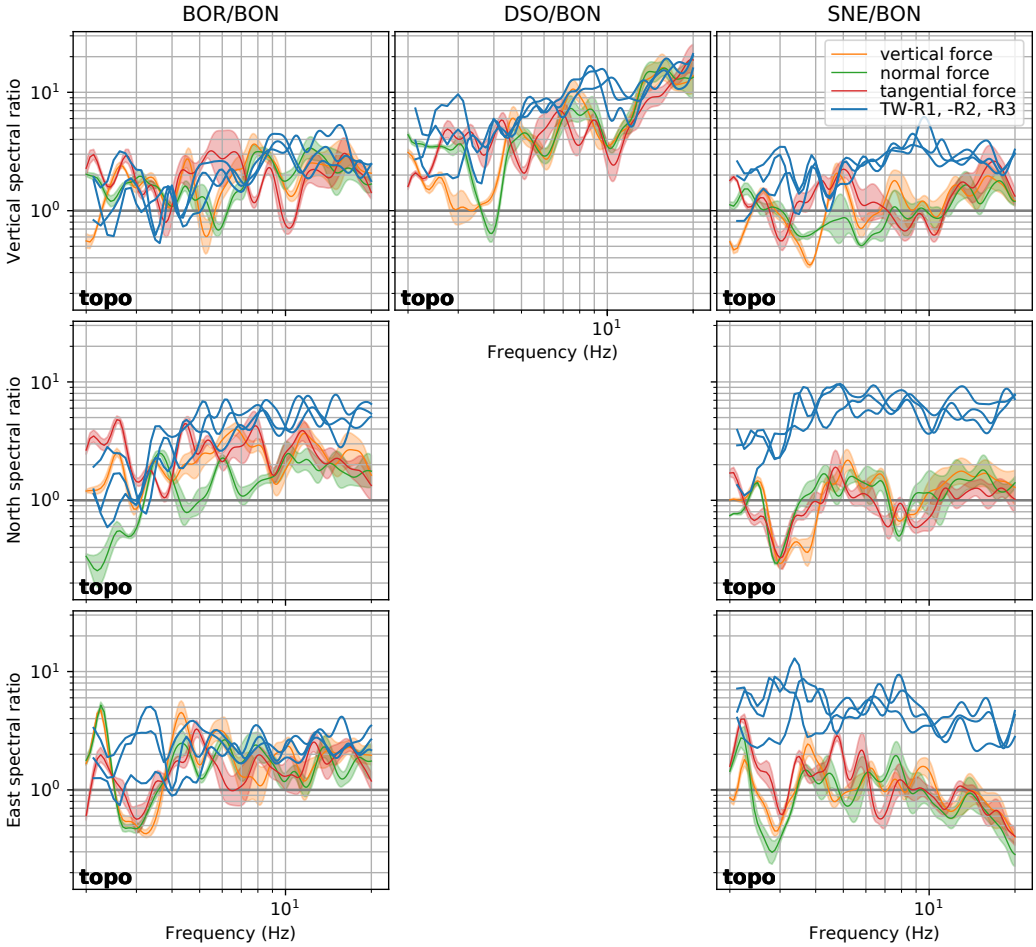

Figure C1. Spectral ratios BOR/BON, DSO/BON and SNE/BON calculated from real signals TW-R1, -R2, -R3 (as in Fig. 10) without site effect deconvolution compared with simulations on domain with Dolomieu topography. Vertical component (*top*), and horizontal components in north- (*middle*) and east- (*bottom*) direction are shown. Simulations are realized with varying source direction: vertical force, force normal to the slope and force tangential to the slope. Shaded zone of the simulated ratios indicate the standard deviation from the mean value of the 7 picked source positions which are indicated in Figure 1 ii).

to be amplified on its vertical component with a peak around 9 Hz. Less evidence of amplification is found for station BOR, except on its north-component which is amplified by a factor of 2 for frequencies above 5 Hz.

Appendix D Observed and simulated spectral ratios for rockfall sources in the southwest

To reinforce the findings of section 5.2.2 that spectral ratios are characteristic to the source position and can be reproduced when the surface topography is taken into account, the same analysis is carried out in the following for rockfall sources located on the southwestern crater wall. Snapshots taken from camera CBOC of the three observed rockfalls are shown in Figure D1, together with the generated seismic signals recorded on the vertical components. At the time of the shown images, all rockfalls are located

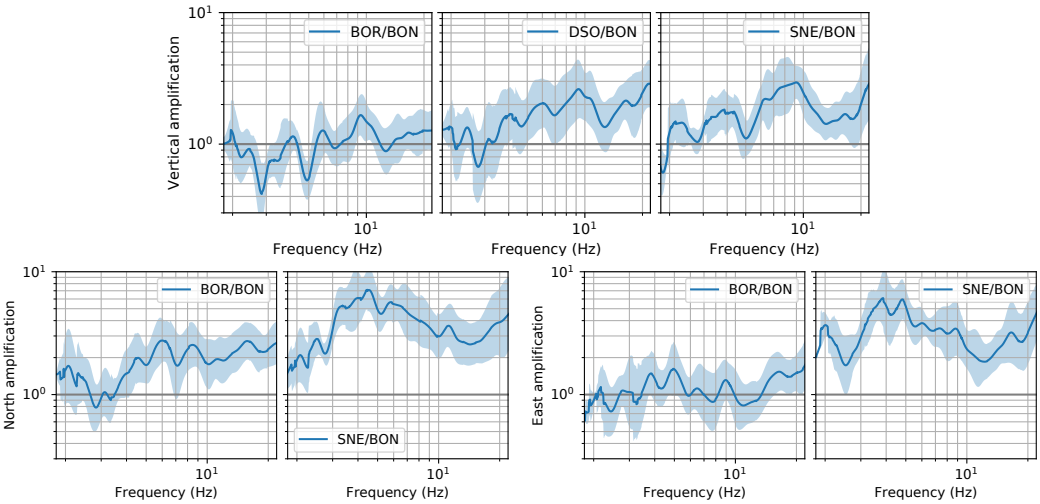

Figure C2. Spectral amplification functions in respect to reference BON for ground velocity of vertical (*top*), north (*bottom left*) and east (*bottom right*) component. Blue shaded zone indicates standard deviation of the amplification distribution from all VTs.

in the same area. The time is marked on the seismic signals by the vertical dotted red lines R1, R2, and R3.

The camera images reveal that each of the rockfalls involves at least two boulders moving downslope simultaneously. Their locations are marked by red ellipses. The associated arrows indicate their direction of movement. We can see that while the boulders of rockfall **1** originate from below the camera position, boulders of rockfall **2** and **3** come from the right hand border of the image. At the time of the snapshot, the trajectories of the three rockfalls cross. At this point the inter-station spectral ratios are compared in order to find out if they are similar according to the similar source location. The spectral ratios are computed from the signals in a window of ±4 s around the time of the shown snapshots. All ratios computed from the observed signals are shown by the blue lines in Figure D2 (note that site effects are already removed here). The graph reveals that the spectral ratios from the three events are again very similar to each other across the whole frequency range for all station pairs, i.e. BOR/BON, DSO/BON and SNE/BON.

The spectral ratios are now compared to simulations from the model with Dolomieu topography. As above, three input force configurations are tested (i.e. a vertical force, a force normal to the slope and a force tangential to the slope in direction of the strongest gradient) to investigate the dependency of the ratios on the source direction.

We can generally observe that the simulated spectral ratios agree very well with the observed spectral ratios. Changing the source direction does not essentially influence the spectral ratios, except for frequencies below 5 Hz which is similar to the observations in Figure 12. The similarity at higher frequencies suggest that the ratios are dominated by the propagation along the topography rather than by the source mechanism. The strongest deviation between observations and simulations at high frequencies is visible on ratio SNE/BON for the east-component. In comparison with the observed spectral ratios, the simulated amplitudes measured at station SNE are strongly underestimated with respect to station BON. This could be be caused by either soil heterogeneities which are not considered in the simulations or by uncertainties of the source position and the fact that the rockfall contains at least two boulders which simultaneously impact the ground.

Analysing the rockfalls located in the southwestern part of Dolomieu crater support the findings from section 5.2.2 that the spectral ratios are characteristic for the source

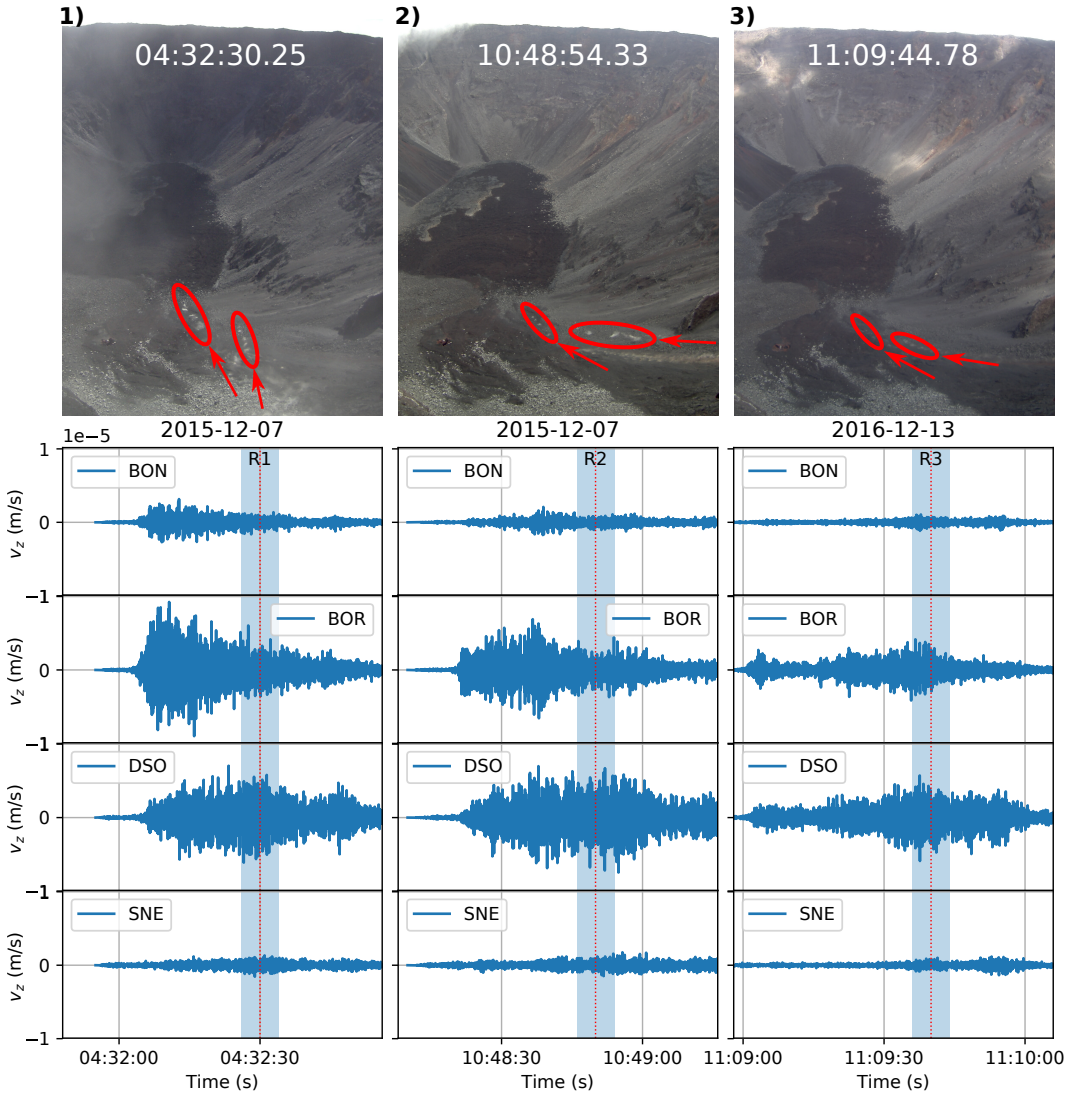

Figure D1. *Top:* Snapshots taken from camera CBOC of three rockfalls at a time for which all rockfalls are in comparable locations. Positions and directions of the boulders are indicated by red circles and arrows. Trajectory of the rockfall on 2016-12-13 is indicated as event **2** on the map in Figure 1 ii) *Bottom:* Corresponding seismic signals (vertical velocity). The vertical dotted lines R1, R2 and R3 mark the time of the camera snapshot shown above. Blue shaded zones display the time windows of ±4 s around R1, R2, and R3 in which spectral station ratios of the signals are computed.

location and can be reproduced when taking into account the surface topography while source direction is not dominant, in particular at high frequencies.

Appendix E Polarization

Polarization analyses can be used for the localization of rockfalls (e.g. Vilajosana et al., 2008; Bottelin et al., 2014). Levy et al. (2018) apply a method proposed by Meza-Fajardo et al. (2015) to extract Rayleigh waves from rockfall seismic signals in order to better evaluate their azimuth of propagation. Working with signals filtered between 2

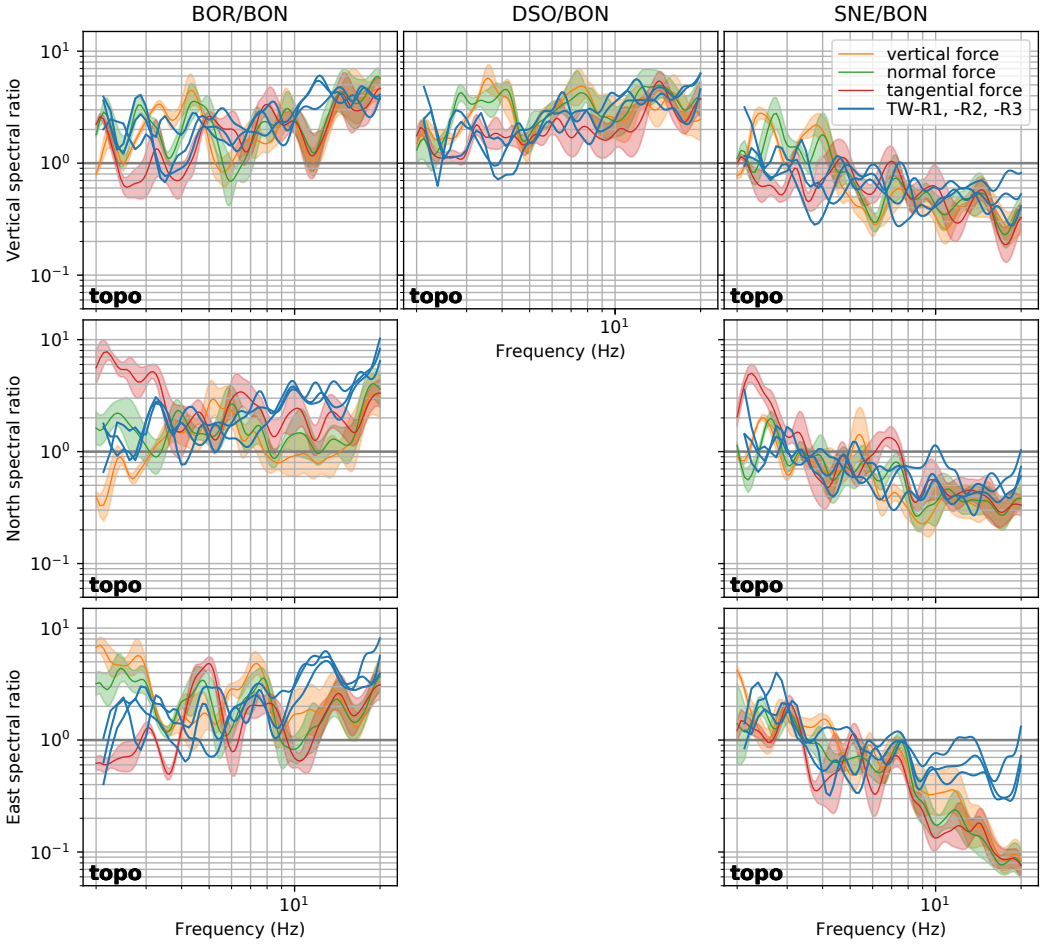

Figure D2. Spectral ratios BOR/BON, DSO/BON and SNE/BON calculated from real signals TW-R1, -R2, -R3 (as defined in Fig. D1) and from simulations on domain with Dolomieu topography for vertical component (*top*), and horizontal components in north- (*middle*) and east- (*bottom*) direction. Simulations are realized with varying source direction: vertical force, force normal to the slope and force tangential to the slope. Shaded zone of the simulated ratios indicate the standard deviation from the mean value of 17 picked source positions located close to index number **2** the trajectory of event **2** on the map in Figure 1 ii).

and 15 Hz, they only find azimuths consistent with theoretical values if i) Rayleigh waves could be extracted with strong certitude, ii) the source-receiver distance is less than 800 m and iii) the station is located on solid rock. They link observed deviations to either complex wave paths or site effects caused by topography and geology.

Here we go further to understand the origins of deviations by analyzing both synthetic and real signals. For this, we investigate the polarization of single wave packets from the single impact N2. As before, the signal is analyzed in a frequency band of 10-20 Hz in order to better separate the wave packets.

At the distant stations BOR and SNE, the signals at this high frequency seem to be too distorted by the long path along the topography so that the polarization analysis does not show any coherent azimuths. This is similar to the problem which is faced by Levy et al. (2018) at far offsets and also in agreement with studies of Ripperger et

al. (2003) and Métaxian et al. (2009) who demonstrate the complexity of particle motions for surface waves traveling along the topography of volcanoes.

On the contrary, the analysis at the closest station BON shows interesting results, which are presented in Figure E1.

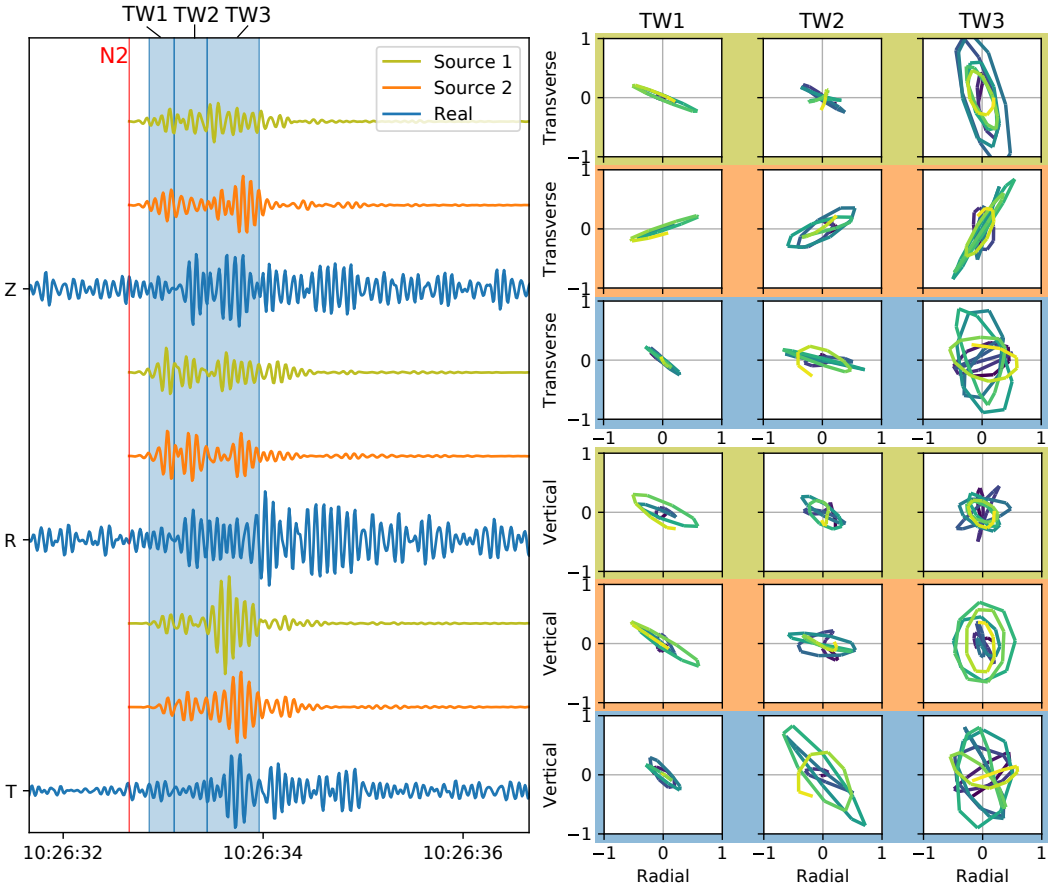

Figure E1. Polarization analysis for simulated and observed signals corresponding to rockfall impact N2. *Left:* Vertical (Z), radial (R), and transverse (T) signal from model with topography (comparison of 2 different source locations 10 m apart from each other) and real recordings. *Right:* Corresponding particle motion in the transverse-radial plane (top) and the vertical-radial plane (bottom).

Shown are synthetics from the model with topography as well as the real signals in terms of vertical (Z), radial (R), and transverse (T) component. Radial and transverse component are defined in respect to the source-receiver direction. To respect the uncertainty on the exact source position, two positions located 10 m apart from each other are compared. Note that the synthetic signals correspond to a source composed by forces normal and tangential to the slope as illustrated in Figure 11. The polarization analysis is carried out in three different time windows.

Investigating the transverse-radial plane (top right of Figure E1), we can observe that the polarization of the simulated signal from source 1 (light green background) is in good agreement with the observations (blue background). Both show similar directions for linear polarized signals in the time windows TW1 and TW2 and a slightly more elliptical polarized signal in time window TW3. Interestingly, changing the source position by just 10 m to source 2 (orange background) switches the direction of the polar-

ization. As the source-receiver azimuth is not significantly changed by this source relocation, the shifting angle has to be explained by influences from the topography. Besides propagation effects from the slightly changing path, the shift is also caused by a change in source direction. This is due to the fact that the source direction is defined in respect to the slope orientation which is slightly different at the new source position.

We learn form this simple polarization analysis that when analysing the polarization of rockfall generated seismic waves it is important to consider not only path effects but also inherent source characteristics. At large offsets, the source characteristics might play a smaller role (similar as we have seen when analyzing the spectral station ratios). Unfortunately, we could not find any meaningful particle motions at large offsets for these high frequencies.

Acknowledgments

We would like to thank Jean-Pierre Vilotte as well as Hugo Martin for fruitful ideas. Thanks to the whole team at the OVPF that provided the excellent data for this study. Seismic and camera data used in this paper were collected by Observatoire Volcanologique du Piton de la Fournaise/Institut de Physique du Globe de Paris (OVPF/IPGP). Seismic data are accessible at the Volobsis website (http://volobsis.ipgp.fr/). Data from cameras and from all simulations are available from the corresponding author upon request. Numerical computations were partly performed on the platform of S-CAPAD (Service de calcul parallèle et de traitement de données en sciences de la Terre), IPGP, France, as well as on the CCIPL (Centre de Calcul Intensif des Pays de la Loire), Université de Nantes, France. This work has been funded by the ERC Contract No. ERC-CG-2013-PE10-617472 SLIDEQUAKES.

References

Ancheta, T. D., Darragh, R. B., Stewart, J. P., Seyhan, E., Silva, W. J., Chiou, B. S., ... Donahue, J. L. (2014). NGA-West2 database. *Earthquake Spectra*, *30*(3), 989–1005. doi: 10.1193/070913EQS197M

Assimaki, D., & Jeong, S. (2013). Ground-motion observations at hotel Montana during the M 7.0 2010 Haiti earthquake: Topography or soil amplification? *Bulletin of the Seismological Society of America*, *103*(5), 2577–2590. doi: 10.1785/0120120242

Bachelet, V., Mangeney, A., De Rosny, J., Toussaint, R., & Farin, M. (2018). Elastic wave generated by granular impact on rough and erodible surfaces. *Journal of Applied Physics*, *123*(4). doi: 10.1063/1.5012979

Battaglia, J., & Aki, K. (2003). Location of seismic events and eruptive fissures on the Piton de la Fournaise volcano using seismic amplitudes. *Journal of Geophysical Research*, *108*(B8), 2364. Retrieved from `http://doi.wiley.com/10.1029/2002JB002193` doi: 10.1029/2002JB002193

Bottelin, P., Jongmans, D., Daudon, D., Mathy, A., Helmstetter, A., Bonilla-Sierra, V., ... Donzé, F. (2014). Seismic and mechanical studies of the artificially triggered rockfall at Mount Néron (French Alps, December 2011). *Natural Hazards and Earth System Sciences*, *14*(12), 3175–3193. doi: 10.5194/nhess-14-3175-2014

Bouchon, M., & Barker, J. S. (1996). Seismic response of a hill: The example of Tarzana, California. *Bulletin of the Seismological Society of America*.

Chaljub, E., Komatitsch, D., Vilotte, J. P., Capdeville, Y., Valette, B., & Festa, G. (2007). Spectral-element analysis in seismology. *Advances in Geophysics*, *48*(06), 365–419. doi: 10.1016/S0065-2687(06)48007-9

Chiou, B. S. J., & Youngs, R. R. (2014). Update of the Chiou and Youngs NGA model for the average horizontal component of peak ground motion and response spectra. *Earthquake Spectra*, *30*(3), 1117–1153. doi:

10.1193/072813EQS219M

Dammeier, F., Moore, J. R., Haslinger, F., & Loew, S. (2011, nov). Characterization of alpine rockslides using statistical analysis of seismic signals. *Journal of Geophysical Research*, *116*(F4), F04024. Retrieved from http://doi.wiley.com/10.1029/2011JF002037 doi: 10.1029/2011JF002037

Davis, L. L., & West, L. R. (1973). Observed effects of topography on ground motion. *Bulletin of the Seismological Society of America*.

Deparis, J., Jongmans, D., Cotton, F., Baillet, L., Thouvenot, F., Hantz, D., ... Hantz, D. (2008, aug). Analysis of Rock-Fall and Rock-Fall Avalanche Seismograms in the French Alps. *Bulletin of the Seismological Society of America*, *98*(4), 1781–1796. Retrieved from https://pubs.geoscienceworld.org/bssa/article/98/4/1781-1796/341946http://www.bssaonline.org/cgi/doi/10.1785/0120070082 doi: 10.1785/0120070082

Derrien, A., Villeneuve, N., Peltier, A., & Michon, L. (2019). Multi-temporal airborne structure-from-motion on caldera rim: Hazard, visitor exposure and origins of instabilities at Piton de la Fournaise. *Progress in Physical Geography*, *43*(2), 193–214. doi: 10.1177/0309133318808201

Dewez, T. J., Nachbaur, A., Mathon, C., Sedan, O., Kobayashi, H., Rivière, C., ... Nowak, E. (2010). OFAI: 3D block tracking experiment on a weathered volcanic rock slope of Tahiti, French Polynesia. *Conf. Procedings, Rock Slope Stability 2010, 24-25 Nov. 2010, Paris, France*.

Duputel, Z., Lengliné, O., & Ferrazzini, V. (2019). Constraining Spatiotemporal Characteristics of Magma Migration at Piton De La Fournaise Volcano From Pre-eruptive Seismicity. *Geophysical Research Letters*, *46*(1), 119–127. doi: 10.1029/2018GL080895

Durand, V., Mangeney, A., Haas, F., Jia, X., Bonilla, F., Peltier, A., ... Villeneuve, N. (2018, oct). On the Link Between External Forcings and Slope Instabilities in the Piton de la Fournaise Summit Crater, Reunion Island. *Journal of Geophysical Research: Earth Surface*, *123*(10), 2422–2442. Retrieved from http://doi.wiley.com/10.1029/2017JF004507 doi: 10.1029/2017JF004507

Farin, M., Mangeney, A., Toussaint, R., Rosny, J. D., Shapiro, N., Dewez, T., ... Berger, F. (2015, oct). Characterization of rockfalls from seismic signal: Insights from laboratory experiments. *Journal of Geophysical Research B: Solid Earth*, *120*(10), 7102–7137. Retrieved from http://doi.wiley.com/10.1002/2015JB012331 doi: 10.1002/2015JB012331

Favreau, P., Mangeney, A., Lucas, A., Crosta, G., & Bouchut, F. (2010, aug). Numerical modeling of landquakes. *Geophysical Research Letters*, *37*(15), 1–5. Retrieved from http://doi.wiley.com/10.1029/2010GL043512 doi: 10.1029/2010GL043512

Festa, G., & Vilotte, J.-P. (2005, jun). The Newmark scheme as velocity-stress time-staggering: an efficient PML implementation for spectral element simulations of elastodynamics. *Geophysical Journal International*, *161*(3), 789–812. Retrieved from https://academic.oup.com/gji/article-lookup/doi/10.1111/j.1365-246X.2005.02601.x doi: 10.1111/j.1365-246X.2005.02601.x

Fuyuku, M., & Matsumoto, Y. (1980). Finite difference analysis of Rayleigh wave scattering at a trench. *Bulletin of the Seismological Society of America*.

Geli, L., Bard, P. Y., & Jullien, B. (1988). The Effect of Topography on Earthquake Ground Motion: A Review and new Results. *Bulletin of the Seismological Society of America*. doi: 10.1016/0148-9062(88)90024-1

Hailemikael, S., Lenti, L., Martino, S., Paciello, A., Rossi, D., & Mugnozza, G. S. (2016, jul). Ground-motion amplification at the Colle di Roio ridge, central Italy: a combined effect of stratigraphy and topography. *Geophysical Journal International*, *206*(1), 1–18. Retrieved from https://academic.oup.com/gji/article-lookup/doi/10.1093/gji/ggw120 doi: 10.1093/gji/ggw120

Harp, E. L., Hartzell, S. H., Jibson, R. W., Ramirez-Guzman, L., & Schmitt, R. G. (2014). Relation of landslides triggered by the Kiholo Bay Earthquake to modeled ground motion. *Bulletin of the Seismological Society of America*, *104*(5), 2529–2540. doi: 10.1785/0120140047

Hartzell, S. H., Carver, D. L., & King, K. W. (1994). Initial investigation of site and topographic effects at Robinwood Ridge, California. *Bulletin of the Seismological Society of America*, *84*(5), 1336–1349.

Herrmann, R. B. (2013, nov). Computer Programs in Seismology: An Evolving Tool for Instruction and Research. *Seismological Research Letters*, *84*(6), 1081–1088. Retrieved from https://pubs.geoscienceworld.org/srl/article/84/6/1081-1088/315307 doi: 10.1785/0220110096

Hertz, H. (1882). Über die Berührung fester elastischer Körper. *Journal für die reine und angewandte Mathematik*, *92*, 156–171.

Hibert, C., Ekström, G., & Stark, C. P. (2014, jul). Dynamics of the Bingham Canyon Mine landslides from seismic signal analysis. *Geophysical Research Letters*, *41*(13), 4535–4541. Retrieved from http://doi.wiley.com/10.1002/2014GL060592 doi: 10.1002/2014GL060592

Hibert, C., Mangeney, A., Grandjean, G., Baillard, C., Rivet, D., Shapiro, N. M., ... Crawford, W. (2014, may). Automated identification, location, and volume estimation of rockfalls at Piton de la Fournaise volcano. *Journal of Geophysical Research: Earth Surface*, *119*(5), 1082–1105. Retrieved from http://doi.wiley.com/10.1002/2013JF002970 doi: 10.1002/2013JF002970

Hibert, C., Mangeney, A., Grandjean, G., Peltier, A., DiMuro, A., Shapiro, N. M., ... Kowalski, P. (2017, mar). Spatio-temporal evolution of rockfall activity from 2007 to 2011 at the Piton de la Fournaise volcano inferred from seismic data. *Journal of Volcanology and Geothermal Research*, *333-334*, 36–52. Retrieved from https://www-sciencedirect-com.insu.bib.cnrs.fr/science/article/pii/S0377027316303195 doi: 10.1016/J.JVOLGEORES.2017.01.007

Hibert, C., Mangeney, A., Grandjean, G., & Shapiro, N. M. (2011, dec). Slope instabilities in Dolomieu crater, Réunion Island: From seismic signals to rockfall characteristics. *Journal of Geophysical Research: Earth Surface*, *116*(4), 1–18. Retrieved from http://doi.wiley.com/10.1029/2011JF002038 doi: 10.1029/2011JF002038

Hough, S. E., Altidor, J. R., Anglade, D., Given, D., Janvier, M. G., Maharrey, J. Z., ... Yong, A. (2010). Localized damage caused by topographic amplification during the 2010 M7.0 Haiti earthquake. *Nature Geoscience*, *3*(11), 778–782. Retrieved from http://dx.doi.org/10.1038/ngeo988 doi: 10.1038/ngeo988

Jeong, S., Asimaki, D., Dafni, J., & Wartman, J. (2019, jan). How topography-dependent are topographic effects? Complementary numerical modeling of centrifuge experiments. *Soil Dynamics and Earthquake Engineering*, *116*, 654–667. Retrieved from https://www.sciencedirect.com/science/article/pii/S0267726117310849 doi: 10.1016/J.SOILDYN.2018.10.028

Johnson, K. L. K. L. (1987). *Contact mechanics*. Cambridge University Press. Retrieved from https://books.google.fr/books?id=Do6WQlUwbpkC{\&}pg=PA45{\&}lpg=PA45{\&}dq=johnson+1885+contact+mechanics{\&}source=bl{\&}ots=gqjfkuec1Y{\&}sig=ACfU3U3{_}MGjPLQugBHMiitM1K3uIUZorZw{\&}hl=en{\&}sa=X{\&}ved=2ahUKEwi3zoSO{_}I{_}lAhUF-YUKHfdoBdAQ6AEwBXoECAkQAg{\#}v=onepage{\&}q=johnson1885contac

Köhler, A., Ohrnberger, M., Scherbaum, F., Wathelet, M., & Cornou, C. (2007, feb). Assessing the reliability of the modified three-component spatial autocorrelation technique. *Geophysical Journal International*, *168*(2), 779–796. Retrieved from https://academic.oup.com/gji/article-lookup/doi/10.1111/

j.1365-246X.2006.03253.x doi: 10.1111/j.1365-246X.2006.03253.x

Konno, K., & Ohmachi, T. (1998). Ground-motion characteristics estimated from spectral ratio between horizontal and vertical components of microtremor. *Bulletin of the Seismological Society of America*, *88*(1), 228–241.

Larose, E., Carrière, S., Voisin, C., Bottelin, P., Baillet, L., Guéguen, P., ... Massey, C. (2015). Environmental seismology: What can we learn on earth surface processes with ambient noise? *Journal of Applied Geophysics*, *116*, 62–74. Retrieved from http://dx.doi.org/10.1016/j.jappgeo.2015.02.001 doi: 10.1016/j.jappgeo.2015.02.001

Lee, S. J., Chan, Y. C., Komatitsch, D., Huang, B. S., & Tromp, J. (2009). Effects of realistic surface topography on seismic ground motion in the Yangminshan region of Taiwan based upon the spectral-element method and LiDAR DTM. *Bulletin of the Seismological Society of America*, *99*(2 A), 681–693. doi: 10.1785/0120080264

Lee, S. J., Komatitsch, D., Huang, B. S., & Tromp, J. (2009). Effects of topography on seismic-wave propagation: An example from Northern Taiwan. *Bulletin of the Seismological Society of America*, *99*(1), 314–325. doi: 10.1785/0120080020

Lee, W. H. K., White, R. A., Harlow, D. H., Rogers, J. A., Spudich, P., & Dodge, D. A. (1994). Digital seismograms of selected aftershocks of the Northridge earthquake recorded by a dense seismic array on February 11, 1994 at Cedar Hill Nursery in Tarzana, California. *US Geol. Surv. Open-File Rept. 94*, *234*.

Lesage, P., Heap, M. J., & Kushnir, A. (2018). A generic model for the shallow velocity structure of volcanoes. *Journal of Volcanology and Geothermal Research*, *356*, 114—-126. Retrieved from https://doi.org/10.1016/j.jvolgeores.2018.03.003 doi: 10.1016/j.jvolgeores.2018.03.003

Levy, C., Helmstetter, A., Amitrano, D., Roy, G. L., & Guyoton, F. (2018, nov). Rayleigh waves in seismic signals of rockfalls. Retrieved from https://hal-brgm.archives-ouvertes.fr/hal-01815453/

Ma, S., Archuleta, R. J., & Page, M. T. (2007). Effects of large-scale surface topography on ground motions, as demonstrated by a study of the San Gabriel Mountains, Los Angeles, California. *Bulletin of the Seismological Society of America*, *97*(6), 2066–2079. doi: 10.1785/0120070040

Maufroy, E., Cruz-Atienza, V. M., Cotton, F., & Gaffet, S. (2015). Frequency-scaled curvature as a proxy for topographic site-effect amplification and ground-motion variability. *Bulletin of the Seismological Society of America*, *105*(1), 354–367. doi: 10.1785/0120140089

McLaskey, G. C., & Glaser, S. D. (2010). Hertzian impact: Experimental study of the force pulse and resulting stress waves. *The Journal of the Acoustical Society of America*, *128*(3), 1087. doi: 10.1121/1.3466847

Métaxian, J. P., O'Brien, G. S., Bean, C. J., Valette, B., & Mora, M. (2009, dec). Locating volcano-seismic signals in the presence of rough topography: wave simulations on Arenal volcano, Costa Rica. *Geophysical Journal International*, *179*(3), 1547–1557. Retrieved from https://academic.oup.com/gji/article-lookup/doi/10.1111/j.1365-246X.2009.04364.x doi: 10.1111/j.1365-246X.2009.04364.x

Meunier, P., Hovius, N., & Haines, J. A. (2008). Topographic site effects and the location of earthquake induced landslides. *Earth and Planetary Science Letters*, *275*(3-4), 221–232. Retrieved from http://dx.doi.org/10.1016/j.epsl.2008.07.020 doi: 10.1016/j.epsl.2008.07.020

Meza-Fajardo, K. C., Papageorgiou, A. S., & Semblat, J. F. (2015). Identification and extraction of surface waves from three-component seismograms based on the normalized inner product. *Bulletin of the Seismological Society of America*, *105*(1), 210–229. doi: 10.1785/0120140012

Mordret, A., Rivet, D., Landès, M., & Shapiro, N. M. (2015). Three-dimensional

shear velocity anisotropic model of Piton de la Fournaise Volcano (La Réunion Island) from ambient seismic noise. *Journal of Geophysical Research B: Solid Earth*, *120*(1), 406–427. doi: 10.1002/2014JB011654

Moretti, L., Mangeney, A., Capdeville, Y., Stutzmann, E., Huggel, C., Schneider, D., & Bouchut, F. (2012, aug). Numerical modeling of the Mount Steller landslide flow history and of the generated long period seismic waves. *Geophysical Research Letters*, *39*(16), 1–7. Retrieved from `http://doi.wiley.com/10.1029/2012GL052511` doi: 10.1029/2012GL052511

O'Brien, G. S., & Bean, C. J. (2009). Volcano topography, structure and intrinsic attenuation: Their relative influences on a simulated 3D visco-elastic wavefield. *Journal of Volcanology and Geothermal Research*, *183*(1-2), 122–136. Retrieved from `http://dx.doi.org/10.1016/j.jvolgeores.2009.03.004` doi: 10.1016/j.jvolgeores.2009.03.004

Pedersen, H., Lebrun, B., Hatzfeld, D., Campillo, M., Bard, P.-Y. Y., Le Brun, B., ... Bard, P.-Y. Y. (1994). Ground-motion amplitude across ridges. *Bulletin of the Seismological Society of America*, *84*(6), 1786–1800. Retrieved from `http://www.bssaonline.org/content/84/6/1786.short{\%}5Cn{\%}3CGotoISI{\%}3E://WOS:A1994QA09700006`

Rai, M., Rodriguez-Marek, A., & Chiou, B. S. (2017). Empirical Terrain-Based Topographic Modification Factors for Use in Ground Motion Prediction. *Earthquake Spectra*, *33*(1), 157—-177. doi: 10.1193/071015EQS111M

Ripperger, J., Igel, H., & Wasserman, J. (2003). Seismic wave simulation in the presence of real volcano topography. *Journal of Volcanology and Geothermal Research*, *128*(1-3), 31–44. doi: 10.1016/S0377-0273(03)00245-2

Sánchez-Sesma, F. J., & Campillo, M. (1993). Topographic effects for incident P, SV and Rayleigh waves. *Tectonophysics*, *218*(1-3), 113–125. doi: 10.1016/0040-1951(93)90263-J

Snieder, R. (1986). The influence of topography on the propagation and scattering of surface waves. *Physics of the Earth and Planetary Interiors*, *44*(3), 226–241. doi: 10.1016/0031-9201(86)90072-5

Soontiens, N., Stastna, M., Waite, M. L., Soontiens, N., Stastna, M., & Waite, M. L. (2013, apr). Numerical Simulations of Waves over Large Crater Topography in the Atmosphere. *Journal of the Atmospheric Sciences*, *70*(4), 1216–1232. Retrieved from `http://journals.ametsoc.org/doi/abs/10.1175/JAS-D-12-0221.1` doi: 10.1175/JAS-D-12-0221.1

Spudich, P., Hellweg, M., & Lee, W. H. (1996). Directional topographic site response at Tarzana observed in aftershocks of the 1994 Northridge, California, earthquake: Implications for mainshock motions. *Bulletin of the Seismological Society of America*, *86*(1 SUPPL. B), 193–208.

Staudacher, T., Ferrazzini, V., Peltier, A., Kowalski, P., Boissier, P., Catherine, P., ... Massin, F. (2009). The April 2007 eruption and the Dolomieu crater collapse, two major events at Piton de la Fournaise (La Réunion Island, Indian Ocean). *Journal of Volcanology and Geothermal Research*, *184*(1-2), 126–137. Retrieved from `http://dx.doi.org/10.1016/j.jvolgeores.2008.11.005` doi: 10.1016/j.jvolgeores.2008.11.005

Vilajosana, I., Suriñach, E., Abellán, A., Khazaradze, G., Garcia, D., & Llosa, J. (2008, aug). Rockfall induced seismic signals: Case study in Montserrat, Catalonia. *Natural Hazards and Earth System Science*, *8*(4), 805–812. Retrieved from `https://www.nat-hazards-earth-syst-sci.net/8/805/2008/` doi: 10.5194/nhess-8-805-2008

Volkwein, A., Schellenberg, K., Labiouse, V., Agliardi, F., Berger, F., Bourrier, F., ... Jaboyedoff, M. (2011). Rockfall characterisation and structural protection - a review. *Natural Hazards and Earth System Sciences*, *11*, 2617–2651. Retrieved from `https://hal.archives-ouvertes.fr/hal-00653458/`

Wang, B., Da, Y., & Qian, Z. (2018). Forward and Inverse Studies on Scattering of

Rayleigh Wave at Surface Flaws. *Applied Sciences*, *8*(3), 427. Retrieved from http://www.mdpi.com/2076-3417/8/3/427 doi: 10.3390/app8030427

Wang, L., Xu, Y., Xia, J., & Luo, Y. (2015). Effect of near-surface topography on high-frequency Rayleigh-wave propagation. *Journal of Applied Geophysics*, *116*, 93–103. Retrieved from http://dx.doi.org/10.1016/j.jappgeo.2015.02.028 doi: 10.1016/j.jappgeo.2015.02.028

Wathelet, M., Jongmans, D., Ohrnberger, M., & Bonnefoy-Claudet, S. (2008, jan). Array performances for ambient vibrations on a shallow structure and consequences over V s inversion. *Journal of Seismology*, *12*(1), 1–19. Retrieved from http://link.springer.com/10.1007/s10950-007-9067-x doi: 10.1007/s10950-007-9067-x

Weaver, R. L. (1982). On diffuse waves in solid media. *The Journal of the Acoustical Society of America*, *71*(6), 1608–1609.

Zhang, Z., Fleurisson, J. A., & Pellet, F. (2018). The effects of slope topography on acceleration amplification and interaction between slope topography and seismic input motion. *Soil Dynamics and Earthquake Engineering*, *113*(May), 420–431. Retrieved from https://doi.org/10.1016/j.soildyn.2018.06.019 doi: 10.1016/j.soildyn.2018.06.019